HHS Public Access

Author manuscript

Adv Mater. Author manuscript; available in PMC 2020 June 01.

Published in final edited form as:

Adv Mater. 2019 June ; 31(24): e1900321. doi:10.1002/adma.201900321.

Near-infrared-II molecular dyes for cancer imaging and surgery

Shoujun Zhu,
Laboratory of Molecular Imaging and Nanomedicine, National Institute of Biomedical Imaging and Bioengineering (NIBIB), National Institutes of Health (NIH), Bethesda, Maryland 20892, United States

Rui Tian,
Laboratory of Molecular Imaging and Nanomedicine, National Institute of Biomedical Imaging and Bioengineering (NIBIB), National Institutes of Health (NIH), Bethesda, Maryland 20892, United States

Alexander L. Antaris,
Department of Chemistry, Stanford University, Stanford, CA 94305, USA

Xiaoyuan Chen, and
Laboratory of Molecular Imaging and Nanomedicine, National Institute of Biomedical Imaging and Bioengineering (NIBIB), National Institutes of Health (NIH), Bethesda, Maryland 20892, United States

Hongjie Dai
Department of Chemistry, Stanford University, Stanford, CA 94305, USA

Abstract

Fluorescence bioimaging affords a vital tool for both researchers and surgeons to molecularly target a variety of biological tissues and processes. This review focuses on summarizing organic dyes emitting at a biological transparency window termed the near-infrared-II (NIR-II) window, where minimal light interaction with the surrounding tissues allows photons to travel nearly unperturbed throughout the body. NIR-II fluorescence imaging overcomes the penetration/contrast bottleneck of imaging in the visible region, making it a remarkable modality for early diagnosis of cancer and highly sensitive tumor surgery. Due to their convenient bioconjugation with peptides/antibodies, NIR-II molecular dyes are desirable candidates for targeted cancer imaging, significantly overcoming the autofluorescence/scattering issues for deep tissue molecular imaging. To promote the clinical translation of NIR-II bioimaging, advancements in the high-performance small-molecule derived probes are critically important. We discuss here molecules with clinical potential for NIR-II imaging, summarizing the synthesis and chemical structures of NIR-II dyes, chemical and optical properties of NIR-II dyes, bioconjugation and biological behavior of NIR-II dyes, whole body imaging with NIR-II dyes for cancer detection and surgery, as well as NIR-II

Among all existing NIR-II fluorophores, the NIR-II molecular dyes are the most remarkable to translate this imaging window into the clinical setting. The advanced NIR-II dyes derived bioconjugates will give doctors an unparalleled view into tissues for tumor detection at greater depths and contrast, allowing early detection during cancer screenings and solid tumor resection by delineation of the boundaries between healthy and cancerous tissues.

fluorescence microscopy imaging. We will also propose a key perspective on the direction of near-infrared-II molecular dyes for cancer imaging and surgery.

Graphiacl Abstract

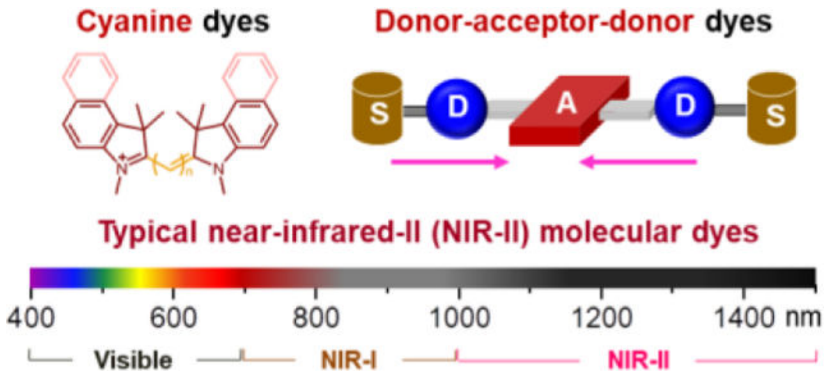

Keywords

NIR-II imaging; NIR-II fluorophore; donor-acceptor-donor dyes; cyanine dye; tumor imaging

1. Introduction

Fluorescence imaging is a remarkable imaging modality for improving disease detection and guided surgery in both research and clinical applications. Compared to radiological imaging techniques, fluorescence imaging offers great advantages with regard to safety and resolution of detection.[1][2] Such a highly sensitive imaging technique allows for investigating the molecular/cellular level activities to understand biological function and disease with the distinct contrast agents.[3] Fluorescence imaging, in particular near-infrared fluorescence imaging (excitation 650–900 nm), provides a new and highly versatile platform for non-invasive molecular imaging.[4] For instance, indocyanine green (ICG) inform surgeons of perfusion levels by allowing visualization of lymphatic vasculature/nodes and cancer stages.[2] Oral Gleolan (5-ALA) recently received orphan drug status for discrimination of malignant gliomas, masses that are notoriously difficult to identify during neurosurgical resection.[5] OTL38 (NIR dye conjugated to folate receptor-alpha (FRa)-targeting ligand) has progressed into phase II/III clinical trials for tumor visualization in lung/ovarian cancers.[6, 7] Bioconjugation of LI-COR's infrared fluorescent dyes (IRDye800CW; λ_{abs} = ~774 nm; λ_{em} = ~789 nm) to a variety of targeting ligands are all in the midst of clinical trials for enhanced tumor visualization in a plethora of cancer types. Finally, activity-based infrared probes, including LUMO15 (Cy5 conjugated to quenching moiety QSY21 through a peptide linker) which fluoresces after cleavage by protease cathepsins that are upregulated in a diverse array of cancers, have completed both feasibility and phase I clinical trials.[4]

To further improve the imaging quality of the NIR fluorescence imaging technique, near-infrared II (NIR-II) biomedical fluorescence imaging was developed recently, providing a highly versatile platform for non-invasive in vivo bioimaging to probe deeper into the

biological tissues/organs with a greater degree of clarity.[4, 8, 9, 10, 11, 12, 13, 14, 15, 16] The current NIR window can be artificially divided into NIR-I (700–1000 nm) and NIR-II (1000–1700 nm, also named as shortwave infrared (SWIR, 1–2 μm)) windows.[17] The NIR-II window can be further classified into NIR-IIa' (1000–1300 nm),[18] NIR-IIa (1300–1400 nm)[19] and NIR-IIb (1500–1700 nm) sub-regions.[20] The dyes discussed in this review include NIR-I dyes with peak emission at NIR-I window and NIR-II dyes with peak emission at NIR-II window. Because the quality of photon attenuation, tissue autofluorescence, and scattering are all significantly reduced when imaging at gradually longer wavelengths, NIR-II fluorescence imaging opens many exciting new imaging avenues for biological research compared to any other optical imaging modality.[4] However, the lack of applicable fluorophores with both high quantum efficiency and biocompatibility causes a dominant barrier on the way to the extensive endorsement of NIR-II bio-imaging in clinical using. Many inorganic and carbon-based nanomaterials, such as single-wall carbon nanotubes,[16, 21, 22, 23, 24, 25, 26] quantum dots,[17, 27, 28, 29, 30, 31, 32, 33, 34, 35] and rare earth nanoparticles,[36, 37, 38, 39, 40, 41, 42] have been developed as NIR-II fluorophores up to present, which bring safety issues with regard to immune uptake and clearance after imaging. Organic fluorophores afford an exceptional alternative, as their fluorescence properties can be controlled by rational chemical structure design, and there are considerable advantages on the subject of biocompatibility and biosafety.[4]

Due to the fact that near-infrared fluorescence imaging can overcome the penetration/contrast bottleneck of visible imaging and the great clinical potential of small-molecule fluorophores, it is a promising imaging method for cancer detection and surgery.[2, 43] A variety of cancer biomarkers have been confirmed as ideal targeted receptors for cancer diagnosis and therapy, such as folate receptor, integrin receptor, epidermal growth factor receptor (EGFR), transferrin receptor, human epidermal growth factor receptor 2 (HER_2) receptor, translocator protein receptor, endothelin receptor, angiogenesis, prostate-specific membrane antigen (PSMA), somatostatin receptor, and gastrin-releasing peptide receptor (GRPR).[44] Due to their convenient bioconjugation with peptide/proteins of interests, NIR-II molecular dyes are excellent candidates for targeted cancer-imaging. These NIR-II probes can significantly decrease the autofluorescence and scattering of deep-tissue molecular imaging in cancer patients. To boost the clinical translation of NIR-II bioimaging, the small molecule derived probes are critically important.[4, 45]

Advanced NIR-II bioconjugates will give doctors an unparalleled view into tissues for tumor detection at greater depths and contrast, allowing, for example, early detection during cancer screenings and solid tumor resection by delineation of the boundaries between healthy and cancerous tissues. Besides summarizing the present developments and proposing a key perspective and future directions, we will particularly compare and balance the benefits of high quantum yields (QYs) of NIR-I dyes and the long wavelength/high contrast of NIR-II dyes. This review contains six sections, including synthesis and chemical structures of NIR dyes, chemical and optical properties of NIR-II dyes, bioconjugation and biological behavior of NIR-II dyes, whole body imaging with NIR-II dyes for cancer detection, as well as NIR-II fluorescence microscopy imaging and future intraoperative NIR-II image-guided surgery.

2. Synthesis and chemical structures of NIR dyes

The photoluminescence of small molecules, controlled by their energy gap (energy separation between the highest occupied molecular orbital, HOMO, and lowest unoccupied molecular orbital, LUMO), is closely related with their chemical structures through π interactions.[46] Researchers have tried to push the emission wavelengths of small molecular dyes to the NIR region by the optimization of structural design and synthetic routes. These diversified NIR dye architectures enrich the library of NIR fluorescent probes through the rational design of backbones and substitutional groups of dye structures. Many forms of NIR dyes, such as cyanine dyes, D-A-D dyes, xanthenes, porphyrins, squaraines, phthalocyanines, and boron-dipyrromethanes, have shown promise in biological systems and tissues with much-improved water solubility, QY, as well as absorption coefficient.[44, 47, 48] However, only cyanine and D-A-D structures have been developed to be NIR-II fluorophores. In this section, we mainly focus on cyanine/polymethine molecules and donor-acceptor-donor (D-A-D) structures.[49, 50, 51, 52, 53] When pursuing an ideal NIR dye, both higher QY and larger absorption coefficient should be taken into account. In addition, discussion of other NIR-I dyes in this section will further force the scientific community to re-design or synthesize their NIR-II derivatives, thus enriching the current library of NIR-II fluorophores.

2.1 NIR-I/II polymethine/cyanine dyes

The adoption of cyanine dyes for NIR in vivo imaging started with indocyanine green (ICG), which has been approved by the US Food and Drug Administration (FDA) for clinical uses in humans.[54, 55] Typical cyanine fluorophores contain two indolenine groups with different numbers of vinylene bonds between them and interchangeable groups. Cyanine dyes have relatively high absorption coefficients, and modified chemical groups allow for further improvement of chemical and optical properties. There are several commercially available cyanine dyes in the NIR-I region including ICG, IR-125, IR-820, IR-830, Cy7.5, DiR, HITCI, IRDye800cw, IR-783, IR12-N3, Cy7, IR-775, IR-780, IR-806, IR-797, IR-140, CF770, Alex Fluo@750, etc. (Figure 1a). The NHS ester, isothiocyanate, succinimidyl ester, maleimide, amine, carboxyl, azide, and alkyne are the most common conjugated versions in part of these commercially available dyes.[1, 56] Through modification with chloro-cyclohexene or polyethylene glycol (PEG), or improved structure, such as octupolar merocyanine and 1,3-bis(dicyanomethylidene)indan of cyanine dyes,[57] the quantum yield and imaging capacity are further improved. Research has confirmed that the installation of a rigid cyclohexenyl replacement in the center could extraordinarily enhance the photostability and QYs of cyanine dyes.[58] The whole class of polymethine dyes with both high extinction coefficients and quantum yields has great potential for clinical implementation.[59, 60, 61, 62]

By prolonging the conjugated structure length and tuning the chemical substitutions, some polymethine structures, such as IR-26, IR-1061, and IR-1048 can fluoresce in the NIR-II window with an emission peak over 1000 nm (Figure 1b–d).[63, 64, 65] Nearly all these molecules are commercially available, and IR-26 has been chosen as a standard to quantify the quantum yields of newly developed NIR-II fluorophores.[66, 67] Cosco et al. used dimethylamino flavylium heterocycles to design novel polymethine dyes (Figure 1e).[63]

These dyes are strikingly red-shifted compared to traditional cyanine dyes, affording a new contrast agent in the NIR-II region. The indication polymethine dye is Flav7, which is almost 13 times brighter than IR-26.[63] The high quantum yield and extinction coefficient of the newly developed polymethine dyes, coupled with the clinical accomplishment of ICG, suggests that polymethine fluorophores hold great potential to translate NIR-II diagnostics into the clinic.

Deng et al. exploited the NIR-Ib imaging of commercially-available cyanine dyes.[68] They found that the screened cyanine dyes (see Table 1) had separate NIR fluorescence peaks in both the NIR-Ia (700–900 nm) and NIR-Ib region (900–1000 nm). In the latest work, Li et al. reported a NIR-II molecular fluorophore FD-1080 by redesigning the cyanine molecules, and the FD-1080 possessed both absorption and emission over 1000 nm (Figure 1b).[69] A sulphonic group and cyclohexene group were modified to increase its aqueous solubility and photo-stability. The NIR-II QY of FD-1080 was tested to be 0.31 % and could be elevated to 5.94 % in FBS buffer. Increasing cyanine NIR-II dyes have appeared in academic literature through structure redesigning or modifying.[70, 71]

By reason of the low quantum efficiency of commonly used silicon spectrometers in >1000 nm window, emission spectra of NIR-I dyes are poorly investigated in the NIR-II region. This results in false emission spectra against Franck-Condon (mirror) rule.[45] Fortunately, the NIR-II tail (>1000 nm) of ICG and IRDye800 was first reported unintentionally by Antaris et al. in Figure S14 of their D-A-D-dye paper (Figure 2a).[72] Further work indicates that the bright tail emission of present NIR-I cyanine dyes (ICG, IRDye800CW, IR-12N3, etc.) can afford high-performance NIR-II imaging.[45, 72, 73, 74, 75] Because the QY of NIR-I dyes is much higher than that of peak NIR-II dyes, it will be very promising to further investigate the tail emission of present NIR-I dyes and screen the optimal fluorophores for accelerating the clinical translation of NIR-II bioimaging.

2.2 Other NIR-I dyes

There are lots of NIR-I dyes which are infrequently used in cancer imaging such as xanthenes, porphyrins, squaraines, phthalocyanines, boron-dipyrromethanes, zwitterionic dyes, and AIE luminogens (AIEgens).[76, 77] Researchers seek NIR dyes with both high extinction coefficients and quantum yields. Koide et al. developed three rhodamine derivatives to facilitate the bioimaging of this type of NIR-I dye.[78] These rhodamine derivatives fluoresced a NIR emission with exciting potential for bioimaging applications. Xanthene/rhodamine dyes are very commonly used dyes, and new generation derivatives span into the NIR region with functional groups controlling their fluorescent emission. Thus, plenty of NIR rhodamine derivatives were exploited by modifying the xanthene core through various strategies to enrich their fluorescence emissions.[79]

Squaraines (squarylium dyes) have a kind of zwitterionic structure with a central ring-based core.[80] Modified oxocyclobutenolate further produces a red or NIR emission. However, the hydrophobic features of such dyes limit their biological applications. Currently, strategies are increasingly developed to adjust the squaraine dyes' NIR emission, regulate the aggregation state, modify the binding moiety, and induce squaraine formation.[81, 82, 83]

Choi et al. investigated that the zwitterionic NIR fluorophore, named ZW800–1, afforded a considerable signal-to-noise ratio (SNR) enhancement compared with IRDye800-CW.[76]

Phthalocyanines and porphyrins, with four isoindole or pyrrole nitrogen atoms, are multifunctional dyes.[84, 85] Their new generation derivatives are favorable in clinical applications for both cancer imaging and theranostics. Porphyrins are specific organic fluorophores with heterocyclic macrocycle, composed of four modified pyrrole subunits. Furthermore, different heterocycles, such as corrins, chlorins, bacteriochlorophylls, and corphins are incorporated into porphyrins. The 5-aminolevulinic acid (5-ALA), is the dominant case of protoporphyrin, and has been widely used for tumor detection and photodynamic therapy in clinical settings.[5]

To address the unavoidable intermolecular aggregation and poor stability of the current commercially-available near-IR dyes, scientists at Nirmidas and Biotium, etc. developed novel structures, resulting in exceptionally bright and photostable dyes.[73, 86] Consequently, a higher number of NIR dyes can be conjugated to a protein for maximal fluorescence, while still preserving conjugate specificity and long in vivo half-life. Based on such diverse structures of NIR-I dyes, much more synthesis work will be needed to establish design rules to exceed their NIR-II derivatives.

2.3 Donor-acceptor-donor (D-A-D) NIR-II dyes

Among all the low band-gap molecules, the donor-acceptor (D-A) types of fluorophores are specifically promising to researchers because their energy gap levels are in tuneable NIR-I/II regions and other properties can be further modified by donors and acceptors. To further lower the energy gap, researchers developed a D-A-D structure with increased electron delocalization to create NIR-II molecules (Figure 3a).[51, 52, 53, 87] The first aqueous-soluble D-A-D dye (CH1055-PEG) was developed by Antaris and Chen et al., serving as a typical model for further design and reconstruction (Figure 3c).[88] For the acceptor groups, benzobisthiadiazole (BBTD), possessing a substantial quinoidal character that allows for improved electron delocalization, is the most popular choice.[50] For the donor groups, thiophene, fluorene, and their derivatives have been adopted to form the D-A-D structure. To make the hydrophobic fluorophores water-soluble, hydrophilic polymer matrices and polyethylene glycol (PEG) were adopted to encapsulate the hydrophobic molecules (Figure 3b).[89] Sun et al. and Ji et al. developed serials of D-A-D fluorophore with redesigning the first-generation CH1055 dyes, and the new generation of NIR-II fluorophore has highly stable and biocompatible features for NIR-II fluorescence imaging (Figure 3d).[49, 90, 91, 92]

To fluoresce in the NIR-II wavelength, NIR-II organic dyes are designed with large conjugated backbones. However, the larger π-conjugated molecules suffer from strong intermolecular interactions and aggregation. As a result, the excited states of such molecules are directly attacked and then quenched by water molecules or oxidative effects. Based on the molecular simulation, the water molecules' interaction with organic fluorophores is the main reason for the reduction of QYs in aqueous media. To address these problems, Yang et al. proposed a shielding unit (S) to D-A-D fluorophores to form new S-D-A-D-S variants (Figure 3b), and dialkoxy substituted benzene/fluorene was predominantly adopted as shielding units in their serial fluorophores.[93, 94] The long side-chains on the fluorene or

benzene extend out of the main backbone thus weaken the molecule-molecule interactions, relieving the aggregation problems. To further optimize the donor groups of such molecules, EDOT (3,4-ethylenedioxythiophene) or TEG substituted thiophene was engaged as the donor to modify the whole structure, serving as efficient support to prevent molecular aggregation. Based on a series of efficient shielding and donor groups, IR-FE was prepared with a fluorescence peak at ~1015 nm and QY of 3.1% in organic toluene. In addition, the PEGylation derivative IR-FEP showed a QY of 0.2% in PBS solutions.[94] Without the donor modification, IR-FTP with single thiophene as a donor only exhibits a low QY of less than 0.01%. In their latest work,[93] the NIR-II fluorophore IR-FTAP with two donors (octylthiophene and thiophene) showed improved optical property with an aqueous QY of 0.53% in NIR-II window (Figure 3e).[95]

Table 1 lists a comprehensive survey of NIR-II dyes, rescaling the quantum yield of all NIR-II peak dyes to the same conservative reference value (IR26 = 0.05%). It clearly indicates the advantage of dual synthesis strategies for fluorophores straddling the NIR-I/II boundary zone. Researchers should strive to supplement the present library of NIR-II imaging dyes by reconstructing and designing similar cyanine dyes.[45] Much more effort should be also provoked to all types of low energy gap molecules, screening the bright NIR-II peak molecule with both high quantum yield and absorption coefficient.

3. Chemical and optical properties of NIR-II dyes

To improve the biomedical applications of NIR-II dyes, numerous chemical routes have been developed to modify the hydrophobic core of the NIR dyes, providing reasonable water-solubility and maintaining the level of brightness as much as possible. Key factors of NIR dyes include water solubility, fluorescence wavelength control, as well as quantum yields enhancement. The biocompatibility belongs to biological behavior which is discussed in the next section.

3.1 Water solubility

The most important issue to address in using NIR dyes in a biological context is water solubility. Small hydrophilic functional groups, such as sulfonate, amine, carboxyl, NHS ester, maleimide, and carboxylate, are modified on NIR dyes to allow for solubility and bioconjugation capacity. Polyethylene glycol with different molecular weights and linear, armed, or branched derivatives, is widely used to modify NIR dyes to obtain good solubility.[88] For most cyanine dyes, sulfo groups are added with classical number one or two, rendering the cyanine dyes improved water solubility, notably, tri-and quadri-sulfonated forms are also available for even higher hydrosolubility. Carboxylate groups are also used to improve the water solubility and biocompatibility of the cyanine dyes; for example, IRDye800CW-carboxylate dispersed rapidly and was completely cleared after 48 h. The water solubility of NIR dyes can also be improved by positive, negative, or zwitterionic charging, given the examples of ICG and Cy7, etc. For most D-A-D NIR-II dyes, PEGylation is the main modification that confers hydrophilicity, not only to the free dyes but also to their labeled conjugate derivates.

Besides the direct chemical modifications, the hydrophobic dyes need hydrophilic encapsulation to be used in *in vivo* experiments or clinical trials, in which the fluorophores perform like nanoparticles, sometimes losing the advantage of small molecules such as in rapid excretion and biosafety. Fortunately, such organic nanoparticles do have the advantage of prolonged blood circulation time, enhanced tumor uptake and drug loading capacity. For example, both polymers and albumin were used to load hydrophobic NIR-I dyes for imaging or therapy applications.[107, 108, 109] Tang' group and Liu' group developed the widely used nanoprecipitation strategy to transfer hydrophobic dye to hydrophilic organic nanoparticles, [105, 110, 111] which has been used in NIR-II fluorophores. Qi et al. reported a stable NIR-II organic nanoparticle by TPA-T-TQ molecule and DSPE-PEG through nanoprecipitation route.[49] Tao et al. adopted polyacrylic acid and DSPE-mPEG to form the IR-1061 nanoparticles for NIR-II imaging.[64] Cheng et al. used both nanoprecipitation and further bioconjugation to achieve the molecular affibody-nanoparticle (DAP), affording both NIR-II and photoacoustic imaging.[96] Shou et al. encapsulated NIR-II fluorophore in phospholipid vesicles to visualize the living circulatory systems and tumor.[97] Water solubility is the prerequisite for clinical translation of NIR-II fluorophores, which needs increasing efforts in terms of structure design, stability assessment, as well as pharmacokinetics test.

3.2 Fluorescence wavelength control

As the fluorescence of small molecules is controlled by the energy gap of the corresponding chemical structures with specific π domains, the emission wavelength can be finely tuned through chemical structure engineering, and there is a balance between the emission wavelength and QY of NIR dyes. Although a longer emission peak could be obtained in NIR molecules with large π domains, the QYs always decrease dramatically from the first NIR to second NIR windows. For example, Cosco et al. developed the new polymethine NIR-II dye (Flav 7) with decreased QY (0.53%, IR26=0.05%) compared with its short-wavelength derivatives (5% for Flav 5). [63]

Commercially accessible NIR-I dyes, with fluorescence emissions centering around the NIR-I region (700–900 nm), were recently proven to own bright NIR-II emission tails, providing a unique opportunity to directly translate NIR-II bioimaging into clinical theranostics (Figure 2a-c).[72, 73, 74, 75] Zhu et al. further found that lots of commercial NIR-I dyes have brilliant emission tails spanning to the NIR-II window, and screened the brightest one, called IR-12N3, which is two-three times brighter than IRDye800/ICG.[73] Very recently, Qi et al. also reported a synthesized fluorophore with NIR-II tail emission by using aggregation-induced emission luminogen (AIEgen), affording an aqueous QY as high as 0.28% (IR-26=0.05%) over 900 nm.[105] Notably, due to the fact that NIR-I dyes always have high QYs, while most of NIR-II fluorophores fall victim to depressed QYs given the inclining of non-radiative electron/hole recombination, the bright NIR-II tail emission will reinvigorate the field of NIR-II imaging with new opportunities. These ground-breaking results afford an immediate route to promote the clinical NIR-II bioimaging.[45]

Zhu et al. systematically investigated the NIR-II emission tail of most commercially available or clinically accessible NIR-I dyes.[73] By screening the tail emission of the most commercially accessible NIR-I dyes with fluorescence centered around 700 to 900 nm, they

achieved the possibility of accelerated preclinical/clinical translation of NIR-II imaging by employing the NIR-II tail emission (Figure 2d-f). The screened NIR-I dyes possessed very brilliant emission tails in the NIR-II window with improved QYs, absorption coefficients, bioconjugation groups, as well as high enhancement factors in serum.[73] The discovery of bright NIR-II dyes will pave the way for a better understanding of biological systems and pathologies by simply replacing the detection camera in existing fluorescence navigation systems, facilitating the transformational potential for a wide range of preclinical or clinical theranostics. Furthermore, the theory modeling data is consistent with the observed NIR-II emission tail. In detail, these cyanine dyes maintain a nearly flat electron distribution in the S_0 state, and with light excitation, middle carbon-carbon bonds of cyanine are elongated, providing the smooth rotation in the process of the S_1 excited state.[73] As a result, the symmetries of the π-conjugated core structure were destroyed and lead to a charge redistribution, further inducing the twisted intramolecular charge transfer (TICT) process (Figure 4).[112, 113] Ensuing the intramolecular twisting, the environment-sensitive TICT S_1 state primarily returns to the ground state through NIR-II (red-shifted) emission.

3.3 Quantum yield enhancement of NIR-II dyes

By optimizing the electron acceptor, π-spacers, electron donors, and substituent groups, the optical properties of organic dyes could change dramatically. Intermolecular aggregation should be avoided in the molecular design. Due to the occurrence of non-radiative electron/hole recombination in NIR-II fluorophores, strategies such as tuning the interactions between NIR dye molecules, coupling with large and hydrophobic π-systems, and the amphiphilic polymer or plasma proteins are efficient routes to design brilliant fluorescent dyes emitting in the NIR-II regions.

Due to the fact that photo scattering and autofluorescence in tissues decrease with longer wavelengths, fluorescence emission at prolonged wavelengths is more suitable for in vivo imaging compared to visible light.[114] As we mentioned in the last section, the low energy gap fluorophores always suffered from the issue of, intermolecular interaction, nonradiative and emission trapping, causing the low NIR-II quantum yield. To reduce the intermolecular interaction between conjugated backbones, several enveloping groups, such as EDOT and dialkoxyl-substituted benzene, were designed to lower the conformational distortion to maintain the rigid structure, enhancing the emission QY in aqueous solutions.[93, 94] By systematically exploring the relationship between donor structure and brightness of D-A-D dyes, Yang et al. achieved an optimal S-D-A-D-S structure. Aside from the single donor structure of D-A-D fluorophores, an extra thiophene (the second donor) was applied to engineer the whole conjugated backbone. Alkyl thiophene serves as a rigid unit to increase the dihedral angle of S-D-A-D-S backbone, resulting in high quantum yields.[95] They also created a computational model to simulate the interaction environment between the designed NIR-II dyes and water molecules. The IR-FTAP was found to possess the least interactions with H_2O in comparison with other screened NIR-II fluorophores, generating the highest QY of D-A-D NIR-II fluorophores (Figure 5).

The capacity for optimizing the structure of D-A-D fluorophores is significantly improved through the use of shielding, donor, and acceptor units.[95] Based on the first water-soluble

NIR-II dye,[88] Sun et al.[92] further modified the CH1055 to increase QY. R1 substituent groups on the fluorene unit are out-of-plane of the π-conjugated system and accordingly avoid intermolecular aggregation and quenching. At the same time, the designed dialkyl substituted fluorene units distort the BBTD backbone to adjust the π-conjugated system. In addition, the fluorene moieties also serve as both the electron donor and shielding groups to avoid aggregation. Based on this design principle, they synthesized three types of NIR-II probes (SXH, SDH, and H1) with improved NIR-II brightness.

It is important that the interaction between NIR-II dyes and proteins improves the brightness of several dyes, due to the formation of H-dimer species at low water concentrations that cause emission quenching. For example, ICG and IR12N3 were found to have 5-fold and 6-fold brightness enhancement from water to serum buffers.[73] A sulfonated CH1055 analog termed CH-4T yielded high binding to serum protein hydrophobic regions, significantly increasing QY by ~110-fold (QY = 1.1%; IR26 = 0.05%) (Figure 6a-e). Wan et al. encapsulated the hydrophobic dye through an amphiphilic polymer polystyrene-poly ethylene glycol (PS-PEG), to produce an ultra-bright NIR-II fluorophore (refer to p-FE, Figure 6f-h).[99, 115] The hydrophobic dye has inherent high QY in the organic solvent,[94] and the absolute QY of the p-FE fluorophore was estimated to be 1.65% (IR26 = 0.05%).

Although NIR-II imaging has been widely reported to have significantly reduced autofluorescence/scattering and deep penetration advantages among different kinds of optical imaging modalities, the “activatable” NIR-II nanoprobe in the NIR-II region is very promising to further promote the contrast resolution and signal-to-background (S/B) ratio.[116] These agents are non-fluorescent or low-fluorescence in the inactivated state, but produce fluorescent after reinvigorating by a specific stimulation. Xu et al. developed dyes@silica nanocomposites (NIR-II@Si), which afford H_2S-stimulated ratiometric emission and illuminate-up the NIR-II light. They used a boron-dipyrromethene dye to produce the NIR-II fluorescence under H_2S activation and the aza-BODIPY fluorophore as the internal reference, serving as the activatable nanocomposite. The activatable nanoprobe can selectively visualize H_2S-rich colon cancer, such as colorectal cancers.[106]

4. Bio-conjugation and biological behavior of NIR-II dyes

Existing NIR-II contrast agents contain a vast number of molecular fluorophores, inorganic QDs and carbon nanotubes, which are mostly used as non-targeted fluorophores. Several molecule-specific probes have been developed in NIR-II regions.[88, 117] For NIR-II macroscopic/microscopic imaging techniques to benefit from the long wavelength region with low autofluorescence and scattering, the evolution of highly targeting NIR-II molecular agents is particularly important.

4.1 NIR-II dyes with conjugation capacity

For most commercially available NIR dyes, many kinds of functional groups are designed to endow them with bioconjugation capacity. Taking IRDye800CW from LI-COR as an example; there are available versions in the forms of NHS ester, azide, alkyne, maleimide, carboxylate, etc. Several high-performance NIR-II dyes (e.g. IR-E1050-COOH, IR-E1050-NH2, IR12-N3, IR-12-NHS) from Nirmidas Biotech also have functional groups for further

bioconjugation. Much research has employed the NIR dyes for targeted staining/imaging and bioassays, by using the functional groups for specific bioconjugations.

Functional NIR dyes were developed in more recent years to target specific cancer types with anti-acceptor bioconjugation. Attaching fluorescent labels to clinical therapeutic antibodies provides a streamlined path through the FDA approval processes for developing the next generation of targeting fluorescent probes. An antibody lightly decorated with 1–2 organic dyes demonstrates a similar pharmacokinetic profile to an unmodified antibody. This signifies that existing FDA-approved therapeutic antibodies minimally modified with advanced NIR fluorescent organic dyes behave similarly in the body relative to the original chemotherapy drug. This reduces the extensive pharmacological testing required if relying on novel targeting structures used in conjunction with a new organic fluorescent dye.

The NIR-II molecule CH1055 was used as a tumor-specific contrast agent by conjugating to a molecular ligand such as an affibody or hormone.[88, 118] In vivo imaging indicated high molecular selectivity of the CH1055-affibody conjugate to an EGFR tumor, with an elevated tumor to normal tissue (T/NT) ratio as high as ~15. Zhu et al. developed a clickable NIR-II molecule (IR-FGP), and copper-free click chemistry utilizing the -N_3 groups on the dye afforded efficient bioconjugation to a wide variety of antibodies and proteins with assistance from a dibenzocyclooctyne (DBCO)-PEG_4-NHS ester linker (Figure 7a).[93] They also developed efficient purification approaches, such as density gradient ultracentrifuge (DGU) separations, given the fact that NIR-II fluorophore conjugates are not compatible with standard purification techniques (Figure 7b). They simultaneously developed an assay analytical method with high sensitivity and high throughput, which was proved to be compatible with cell staining protocols (Figure 7c-d).

In their further work, Zhu et al. developed a bright carboxyl NIR-II dye (IR-FEPC), which was ~9 times brighter than the previously reported CH1055.[18] After optimizing the conjugation conditions of IR-FEPC and ovary hormone (hCG) in several reaction buffers, a high-performance hCG conjugate was achieved. By using their home-built NIR-II confocal technique with the one-photon approach, this new bioconjugate facilitated the 3D mapping of whole ovaries without tissue clearing techniques and achieved an unprecedented 900 μm scanning depth (the deepest record using such a technique to date).

There are lots of well-established cancer cell markers that could carry the conjugated fluorophores to target specific cancer, playing important roles in imaging guided-surgery and therapy. The most widely used NIR-II molecular imaging relies on antibody-derived probes. Compared to antibodies with large molecular weights and sizes, peptides, with their competitive targeting efficiency, could afford extra rapid clearance ability. By developing a novel peptide (CP) specific to tumor stem cell biomarker CD133, Wang et al. reported that the renal excretion peptide-NIR-II dye conjugate allowed for high performance in vivo with tumor targeting ability.[100] In addition, the developed probes could be rapidly renally excreted, in sharp contrast to the typical antibody-based conjugate with high liver accumulation.

4.2 NIR-II dyes with renal/hepatobiliary clearance capacity.

Small molecules and their derived metabolites are proven to be excreted from the body through urine and/or bile.[119] Researchers have conducted systematic studies in live animals by isolating tissues and cells, and have concluded that disparate transport systems might be accountable for the transport of different types of organic molecules, including small, large, anionic, and cationic compounds.[119, 120] Due to the complicated excretion pathways of different materials, only a general rule can be presented: small and hydrophilic molecules are excreted preferentially through urine whereas large and amphipathic molecules are excreted predominately through the liver/bile.[45]

For both NIR-I and NIR-II dyes, the most important aspect of potential clinical translatable imaging or mapping is fast clearance with minimal retention in non-targeted organs after injection and imaging, by either the hepatobiliary clearance or renal excretion pathway in preference. The reported IRDye800CW (and other non-sulfonated cyanine dyes) and some of the D-A-D NIR-II dyes are usually cleared via renal excretion, owing to their low binding affinity with serum proteins and small molecular weights. PEGylation affords additional advantages in lowering liver/skin uptake.[107, 120] The relationship between chemical structure and excretion mechanism needs a systematic investigation to enrich the present library of fast clearance NIR-II dyes.

The paucity of excretable organic dyes similar in properties to their shorter wavelength FDA-approved counterparts has hindered the prospects of clinical imaging in the NIR-II biological transparency window until recently. Above mentioned CH1055-PEG is a rapidly excreted NIR-II dye, 90% of which can be eliminated renally less than 24 h (Figure 8a and d).[88] Zhang et al. reported an improved D-A-D dye with renal excretion capacity and imaged traumatic brain injury (TBI) in the NIR-II window (Figure 8b).[98] Very recently, Wang et al. and Wan et al. reported a renal excretion NIR-II dye with QY as high as 1.5% and developed a renal excretion peptide-dye conjugate (Figure 8c).[100, 101]

To figure out the excretion mechanism among NIR-II dyes, Tian et al. systematically investigated several key NIR-II dyes and found that the liver uptake of NIR-II dyes has a positive correlation with macrophage uptake.[102] Although some NIR-II dyes have very high binding affinities between proteins, the high macrophage uptake is the key factor for liver accumulation. They concluded that renally-excreted NIR-II dyes should have small hydrated size, electroneutral chemical structure, fast dissociation with proteins, and low macrophage uptake. This screened rule is very important to guide the efficient synthesis of renally excreted NIR-II dyes.

4.3 Biocompatibility of NIR-II fluorophores

Although the water solubility and renal/hepatobiliary excretion are very important to apply NIR-II fluorophore to in vivo imaging, they are only the prerequisites and further addressing the biocompatibility is the key point to clinical translation of fluorophores. Different from medical devices and therapeutic materials, imaging agents have a specific definition of biocompatibility. According to Wikipedia and Williams' definitions,[121, 122] the biocompatibility refers to "the quality of not having toxic to biological systems, or the

ability of a fluorophore to behave with an appropriate body response in a specific application, without undesirable local or systemic effects." As a result, to fully evaluate the biocompatibility, the synthesized materials have to first pass several standard in vitro tests, such as those described in the International Organization for Standardization (ISO) 10993 protocols. After proving the in vitro biocompatibility, the animal testing and clinical trials will be performed in sequence.

The current reports on NIR-II fluorophores are only limited to preliminary pharmacokinetics study. Using NIR-II signal to locate the fate of NIR-II fluorophores in living body or organs is much straightforward but lacking sufficient accuracy. An improved or alternative strategy has to be developed to solve this issue. Moreover, the administrated dosing and adverse effects have to be considered and systematically optimized. Because the NIR-II fluorophores are used for intravenous, subcutaneous or intramuscular injection for several kinds of imaging, the in vitro and in vivo toxicology testing should be conducted before any first-in-man study or clinical trials. The principle of structure design or modifications to improve the biocompatibility of NIR-I dyes should also be adopted in the synthesis of NIR-II dyes.[107, 123] Even that FDA-approved ICG could be repurposed to be NIR-II fluorophore, we still need much effort to translate other high-performance NIR-II fluorophores into the clinic.

5. Whole body cancer imaging with NIR-II dyes

With the advent of NIR-II dyes, researchers can visualize deep anatomical features with fantastic clarity. After laser excitation, optical NIR-II photons travel nearly unperturbed through the body with minimal autofluorescence signal generated by the surrounding tissues. NIR-II photons, compared to their traditional visible and NIR-I counterparts,[124, 125] are less attenuated or scattered during their journey out of the body. The combination of minimal light-tissue interactions and low background noise provides a clear view deep into the body, capable of extraordinarily high signal-to-background ratios that are only achievable when moving from the NIR-I to NIR-II region. Using NIR-II organic dyes with imaging systems capable of detecting their low energy emitted photons, researchers have achieved optical penetration depths up to 1 cm and micron-scale resolution imaging of anatomical features that are otherwise unresolvable with traditional fluorescence imaging.[18, 99, 105] This has enabled non-invasive, through-the-skin/skull imaging of the mouse cerebral cortex, real-time subdural visualization of blood hemodynamics in response to traumatic brain injuries, and deep tissue tumor detection with unprecedented signal-to-background ratios.

5.1 Cancer detection

Fluorescence imaging is a powerful tool that allows researchers and physicians to peer directly inside biological tissues.[1] For in vivo fluorescence cancer detection, nonspecific and cancer targeting agents are currently available.[126] These methods have been used to detect cancer by measuring biomarker expression levels.[59] Traditional medical fluorescence imaging uses wavelengths spanning the visible (400–700 nm) region of the electromagnetic spectrum. These wavelengths, however, display poor optical penetration

depths as well as high levels of photon scattering and background autofluorescence. As a result, traditional medical fluorescence imaging cannot effectively resolve features below the surface of the skin (~0.4 mm penetration depth). High photon scattering when traveling through tissues at these wavelengths causes physiological features to appear blurry or out-of-focus when imaging deeper into the body. Additionally, the high background tissue autofluorescence surrounding fluorescently labeled anatomical structures results in low image contrast that reduces doctors' ability to positively identify a feature of interest.

NIR-II targeted imaging for cancer detection has been explored in several papers. Antaris et al. applied a NIR-II dye@affibody conjugate to a test head and performed NIR-II imaging-guided surgery (Figure 9).[98] Although PEGylation of CH1055 produces the renally excreted NIR-II imaging contrast agent, CH1055 with carboxyl groups could function with more tumor-specific targeting ability by linking to an affibody. When the CH1055@affibody conjugate was injected into squamous cell carcinoma (SCC) tumor-bearing mice at a suitable post-injection time point, the tumor position signal could be distinguished with a T/NT ratio as high as 15, which is a five-fold increase compared to NIR-I imaging with a similar affibody and tumor model.

Sun et al. conjugated the NIR-II fluorophore H1 with an RGD peptide and investigated targeted tumor imaging in U87MG tumor-bearing mice (Figure 10).[91] The U87MG tumor was visualized at 24–72 h post-injection time points, with the maximum signal at 48 h. An RGD blocking experiment was additionally conducted to prove the specificity of H1@RGD for the integrin $\alpha_v\beta_3$ receptor. The follow-up *ex vivo* biodistribution study indicated that the liver and kidneys possessed the highest conjugate uptake, indicating the combination clearance routes of both the hepatobiliary and renal systems of the H1@RGD conjugate. The *ex vivo* NIR-II signal indicated that the uptake of H1@RGD in tumors was higher than in other normal tissues except the liver/kidney, confirming the excellent integrin $\alpha_v\beta_3$-targeting ability.

Wang et al. developed CD133 conjugated NIR-II probes for *in vivo* tumor imaging. A new CD133 peptide (CP) was screened for high affinity/specificity. CP based NIR-II probe (IRT) was developed as CP-IRT, which was employed to realize high-resolution $CD133^+$ tumor imaging with high SBR and specificity. CP-IRT is a peptide-conjugated small molecular probe for targeted tumor imaging which demonstrates renal excretion behavior with minimal toxicities and low organ uptake. Compared to the antibody-modified IRT, which revealed high uptake in the liver, CP-IRT showed quick renal excretion behavior. As a result, CP-IRT probes showed the potential for clinical use.

The NIR-II tail emission of commercially available NIR-I dye was also investigated as molecular imaging in the SCC tumor with Erbitux@IR-12N3 conjugate.[73] The tumor was observed with the highest signal accumulation compared with other organs in broad NIR regions. The uttermost T/NT ratio was quantified statistically as ~4 in NIR-I window and ~10 in NIR-II region, demonstrating the superior contrast improvement spanning the imaging from NIR-I to NIR-II windows. Moreover, the IR-12N3 derived NIR-II molecular imaging also eliminated the disadvantage of typical D-A-D dye based molecular imaging, which has unavoidable liver uptake. Due to the highly relevant of the cyanine dye with

clinical imaging set-up, the increased imaging contrast from NIR-I to NIR-II windows with the same probe system exhibit extraordinary promise for intraoperative navigation surgery.

5.2 Vessel imaging of tumor development

Cancer imaging is an important method for early detection and imaging-guided surgery. Except for targeting cancer cells, imaging of small vessels plays a crucial role in investigating and understanding the tumor microenvironment. Several significant findings have emerged from recent applications of advanced vessel imaging methods. Vascular imaging in real time manner that equips both anatomic and hemodynamic information will extremely facilitate the cancer detection and accurate assessment of therapeutic effects.[127] NIR-II fluorophores have been successfully applied in monitoring tumor vessels *in vivo*, showing great penetration depth and micrometer spatial resolution.

As mentioned above, Wan et al. developed an ultrabright NIR-II complex p-FE (hydrodynamic size is 11 nm) through the hydrophobic dye and amphipathic polymer (PS-PEG).[99] They further performed a three-dimensional (3D) vessel imaging in the mouse brain with the home-built NIR-II confocal set-up.[99] Benefited from both high brightness of the developed fluorophore and deep penetration of NIR-II imaging, they achieved an unprecedented 3D vessel imaging with one-photon NIR-II technique. Tiny vessel with 5–7 μm width could be visualized with great contrast while the imaging depth can be as deep as 1.3 mm (Figure 11). They further performed the tumor imaging through the well-known enhanced permeability and retention (**EPR**) effect and prolonged circulation time of the p-FE nano-complex. After tail-vein administration of p-FE, the 4T1 tumor was lighted up over time and accumulated to peak at two days time points with the T/NT ratio as high as ~12. The high brightness and tumor uptake allow real-time imaging with short exposure time (1 ms for 1200 nm long pass window and 5 ms for 1300 nm long pass window). It will be great if there are two dyes with disparate emission in NIR-II window, which could be used as dual-color imaging agents, however, there are still no successful reports on longer emission of aqueous soluble NIR-II dyes over 1500 nm. In current reports, laser-ablation produced carbon nanotubes (CNT) and lead sulfide QDs with emitting in the NIR-IIb window were used to combine with NIR-II dyes to achieve dual-color NIR-II imaging. For example, Wan et al. lighted up the tumor with laser-ablation CNT and vessels with the p-FE fluorophore (**Figure S12**) simultaneously.[99] Zhu et al. achieved dual-color imaging follicle stimulating hormone (FSH) and human chorionic gonadotropin (hCG) receptors in the mouse ovary with a NIR-II dye in 1100–1300 nm window and lead sulfide QDs in over 1500 nm window.[18]

5.3 Lymphatic imaging for cancer diagnostics

The exact detection and identification of lymph nodes by direct imaging approaches have essential therapeutic and prognostic significance for cancer diagnostics. Although current cross-sectional imaging modalities can detect the large size of lymph nodes, due to the fact that the metastases could be existing in non-enlarged lymph nodes and not all enlarged nodes are malignant, the nodal metastases are prone to exaggerated prognoses in patients. NIR-II fluorescence imaging affords the possibility to solve this resolution-limited issue, while PET is still constrained by the limitations of current resolution for small nodal metastases. Compared to multifarious imaging techniques and modalities, optical imaging is

a promising intraoperative technique. Using NIR-II imaging agents and robot-assisted surgery, surgeons will be able to find efficient routes for many kinds of surgical operations, relying on visual cues of the imaging set-up instead of tactile feedback by the naked eye.

Optical navigation surgery has been performed in NIR-I regions with several successful surgical guided set-ups.[103, 104, 128] However, Imaging the deep lumbar lymph nodes is always challenging for optical imaging. By stretching the mouse body to narrow the space between the lumbar lymph nodes and body surface site, NIR-II imaging can visualize two lumbar lymph nodes while NIR-I imaging fails to capture these structures. NIR-I/II lymph node imaging was achieved with the NIR-I/II dye IR-12N3 in nude mice. IR-12N3 based NIR-II imaging of mouse lymph nodes promoted an improved lymph node-to-background ratio, which was 5 fold greater than that in the NIR-I region with significantly clearer lymph node lineaments.[73] The superior lymph node imaging by NIR-II tail emission of IR-12N3 with incredible imaging contrast is paralleling the image quality of the same lymph node through previous D-A-D dyes (Figure 13a–g).

ICG has found a great application in accurately mapping sentinel lymph nodes (SLN) for specific surgical resection, which is under several clinical trials. Selectively cutting sentinel lymph nodes decreases lymphoedema, which can be used to prevent tumor metastasis. Clinicians used ICG to monitor the lymphatic vessels draining the tumor, coupling with the sentinel lymph nodes. Antaris et al. achieved the lymphatic vasculature system, lymph node, and lymphatic draining tumor imaging in U87MG tumor-bearing mice (Figure 13h–k).[88] Their S/B ratios of lymphatic vasculature exhibited a much sharper structure in a CH1055-PEG injected mouse compared to the ICG one in the NIR-I window, with lymph node SBR improved by nearly a factor of two. In sharp contrast to ICG with low tumor uptake, interestingly, strong tumor uptake was observed in a CH1055-PEG injected mouse with the T/NT ratio up to ~5 at the 24 h post-injection time point.

5.4 Clinical potential of the NIR-II emission tail of NIR-I dyes

The importance of ICG's NIR-II emission tail should not be understated, as ICG-based near-infrared imaging in becoming the standard of care in many surgical procedures. For instance, based on the multi-institutional PILLAR II clinical study findings,[129] ICG fluorescence angiography provides an indicator of tissue health during left-sided colectomy and anterior resections. Intraoperative ICG tissue perfusion visualization routinely modifies surgical planning to prevent catastrophic anastomotic leak complications. Fluorescent biliary tree delineation during cholecystectomies has identical success to intraoperative x-ray based cholangiography;[130] clear cystic/hepatic duct identification shows promise for reducing the ~0.5% bile duct injury rate in minimally invasive surgery. The National Comprehensive Cancer Network (NCCN) recommends fluorometric sentinel lymph node (SLN) mapping in endometrial cancer via direct cervical ICG injections.[131] Extracting pelvic/para-aortic sentinel lymph nodes, which are 3-fold more likely than non-SLN to harbor tumor metastases, provides accurate staging for optimizing postoperative patient care. Finally, ICG entrapment in cytokeratin 7-positive hepatocytes compressed by colorectal liver metastases highlights an emerging,[132] innovative visualization strategy for millimeter-sized tumors that are easily missed in hepatic resections. Optically filtering ICG's NIR-II photons should

improve upon optical penetration depths, feature size resolution, and signal-to-background ratios in these and a whole host of other ICG surgical applications. For instance, NIR-II ICG imaging may allow for deeper, finer structural imaging in higher BMI patients while improved ICG tumor-to-background ratios may increase colorectal liver metastases identification. Giving surgeons the intraoperative ability to tune to specific fluorescent detection bands in the NIR-I/II wavelength regions should tailor visualization to specific surgical tasks.

Exploiting the long NIR-II emission tails of NIR-I dyes provides an interesting new preclinical synthetic approach for the next generation of NIR-II emissive fluorophores. While both cyanine and polymethine-based dyes (ICG, IR12-N3 and IRDye800CW) display intrinsic NIR-II emission tails, iterative side chain modifications, as well as new functional core structures should continue to improve upon NIR-II emission levels. Spectroscopic analysis of all molecular fluorophores that straddle the division between the NIR-I/II regions on both silicon and InGaAs detectors may provide further insight into additional dye classes with elevated NIR-II emission levels. Innovative new approaches, which include utilizing a 7-dimethylamino flavylium heterocycle to construct a polymethine dye library in the NIR-I/II regions, require further investigation as off-peak NIR-I dyes may possess stronger NIR-II emission levels than peak NIR-II dyes. Other NIR-I dye structures, such as xanthenes, porphyrins, squaraines and boron-dipyrromethanes,[43] require deep reinvestigation in the near future to obtain additional dye classes with strong NIR-II emission tails. To expedite clinical translation, NIR-I peak dyes currently within or starting clinical studies including ZW800–1, IS001, and IRDye800 derivatives should undergo careful InGaAs/silicon spectral analysis. Reassessing both NIR-I and NIR-II optical characteristics may uncover a clinical NIR-I dye with superior NIR-II performance relative to ICG/IRDye800CW.

6. NIR-II microscopy imaging and future intraoperative NIR-II image-guided surgery

With the well-established library of NIR-II fluorophores and bioconjugate derivatives, we have great opportunity to develop NIR-II imaging set-ups for both lab-scale and/or clinical use. We mainly discuss the NIR-II microscopy imaging and potential intraoperative NIR-II imaging-guided surgery in this section. Because of the significant decrease of tissue autofluorescence and scattering, NIR-II based microscopy imaging and guided surgery will afford much-improved penetration depth and accuracy.

6.1 NIR-II microscopy imaging

Progresses in *in vivo* fluorescent imaging of biologically relevant entities in the NIR-II region allow for probing deep tissues with elevated resolution. However, most reports on NIR-II fluorescence imaging acquired images in a wide-field imaging set-up, in which images were captured as two-dimensional (2D) surface-weighted, epifluorescence photographs that contained insufficient depth information for 3D reconstruction and rendering of volumetric images. Moreover, imaging set-up based on the wide-field route generally superimposes the signal onto the two-dimensional plane, reducing the imaging resolution and the penetration depth. In contrast, confocal imaging can record signals

through a tiny pinhole and reject out-of-focus signals, allowing for a three-dimensional mode imaging. However, a specification for confocal imaging is the highly selective targeting of the fluorophore, which is required to perform 3D imaging with sufficient resolution to obtain the feature of interest. Targeted molecular imaging allows for better sensitivity/specificity, considering that the un-conjugated NIR-II dyes result in high nonspecific background signal.[18]

There are also several home-built fluorescence platforms for high resolution and high contrast live imaging.[18, 133, 134, 135] We summarize two key NIR-II microscopy set-ups and their advantages in visualizing the tumor microenvironment with sub-cellular resolution. Super-resolved fluorescence microscopy, two-photon microscopy, light-sheet microscopy, and NIR-II confocal microscopy are also expected to be combined with suitable NIR dyes, providing the possibility to observe the whole tumor heterogeneity.

To collect quality NIR-II imaging with high resolution in the micrometer scale, Dai's group built a NIR-II confocal microscope based on the NIR-II sensitive detector and optical parts. The scheme of the home-built confocal microscope was shown in Figure 14a;[18] in short, the excitation laser (green, 785 nm in their report) went through the excitation filter, dichroic, and finally into the 100X objective. With excitation of the NIR-II probes, the emission signal of the scanned samples went back from the objective. The short-pass dichroic filter placed in the excitation route can reflect the emission light, which was labeled as the pink beam in Figure 14a. The reflected signal was then focused onto the pinhole several μm in size and passed through an emission filter. The collected signal with high focus finally went into the photomultiplier diode (PMT). Based on their high performance, NIR-II conjugate and the developed NIR-II high-resolution confocal microscopy performed three-dimensional NIR-II imaging with μm resolution and detected three particular ovarian stages with theca, granulosa, and luteal enriched cells, respectively (Figure 14b-c). The penetration depth can reach around 1000 μm. They further built a NIR-II light sheet microscopy (LSM) with optical excitation and detection wavelengths up to 1320 and 1700 nm respectively. The frame-to-frame imaging route afforded a much-improved scanning rate and can visualize never-before-seen dynamic biological processes.[134]

Observing deep tissue information in vivo at a (sub)cellular resolution to explore the molecular signals and cell behaviors is a critically important direction for both oncology and other biological processes. Intravital imaging, affording quantitative and dynamic visualization/mapping into tumor biology and immunology, has realized this goal,[136] with the help of the long-term imaging windows (cranial window, dorsal skinfold chamber, the mammary window, as well as abdominal window).[137] There are several reports regarding the intravital imaging of the tumor microenvironment.[137, 138, 139] We expect that NIR-II intravital imaging will create a dramatic chapter of tumor microenvironment imaging with deep penetration, high resolution, and three-dimensional capacity.

6.2 Future intraoperative NIR-II image-guided surgery

The reduced tissue autofluorescence and scattering are the motivation for developing NIR-II fluorescence-derived biomedical imaging (Figure 15a-b). Whether for laparoscopic or open surgery, all clinical camera systems rely on a silicon semiconducting active layer for

converting visible/NIR-I photons to electrical energy. Silicon charge-coupled devices (CCD) and complementary metal-oxide semiconducting (CMOS) detectors accumulate charge in response to incident photons in the range of 300–1000 nm. After 1000 nm, silicon's quantum efficiency drops precipitously (< 5%), disallowing detection of NIR-II-emissive fluorescent probes. Fortunately, other semiconductors including indium-gallium-arsenide (InGaAs) provide high quantum efficiencies (QE = 70–80%) up to ~1700 nm, with certain proportions of InAs/GaAs facilitating detection past 2.4 μm. InGaAs, a direct low band-gap semiconductor, is predisposed to high dark currents owing to ambient thermal energy populating the conduction band with electrons (Figure 15c). This requires daily liquid nitrogen cooling for older generation InGaAs cameras. However, newer InGaAs sensors, vastly improved as a result of industrial/military remote sensing technology and operate at temperatures of only −60 to −30 °C, a feat achievable solely with thermoelectric cooling. A variety of commercial InGaAs cameras capable of low energy NIR-II photon detection show promise for incorporation into clinical imaging hardware.

The discovery that NIR-I dyes (ICG/IRDye800CW/IR-12N3) displays long emission tails reaching into the NIR-II region highlights potential deficiencies in photospectrometer characterization past ~ 900 nm. These discrepancies serve as a cautionary tale for optical characterization in regions of low silicon sensitivity. Disparate fluorophore emission levels in this region have far reaching implications; for instance, ICG's labeling package insert across commercial dye manufactures incorrectly shows negligible fluorescent emission at 900 nm. ICG's chronic fluorescence underrepresentation past ~900 nm in academia/industry speaks to the fact that optical spectroscopy at wavelengths where silicon's absorption coefficient drops precipitously requires careful consideration. Organic dye designers must take into consideration that emission spectrums are corrected by the underlying semiconducting active layer's spectral sensitivity; while silicon sensors typically yield a relatively flat response in the visible region, sensor electrical responses are corrected by larger factors to account for decreasing photon NIR-II/SIWR responses. These recent results highlight the importance of spectral analysis on both silicon and InGaAs sensors for understanding the true optical properties of NIR fluorophores.

Current NIR-I fluorescence navigation systems show a division between open imaging platforms (e.g., Novadaq Spy, SurgVision, FLARE, Photodynamic Eye, GXMI Navigator, Fluobeam, SurgOptix) and endoscope-based systems (e.g., Novadaq Pinpoint, da Vinci endoscopes, Stryker, Storz, Artemis) for laparoscopic/robotic surgery.[62, 140] Innovations in fluorescent imaging hardware and display technology have kept pace with new fluorophore chemistry and molecular targeting advances. These include full-color infrared imaging (co-located NIR and white-light endoscopic image), intraoperative quantification of fluorescent signal intensity, and augmented reality displays such as Microsoft HoloLens which overlay fluorescence onto the surgical scene after co-registration. Continued innovation in vision engineering can produce instrumentation that supports both ICG and IRDye800CW. By simply switching the detection camera in existing fluorescence navigation systems, we anticipate that the bright NIR-II tail emission of the clinical NIR-I dyes will boost the clinical translation of NIR-II imaging techniques. A fluorescence navigation system with tunable detection bands spanning the NIR-I to NIR-II range could further support

multiplexed fluorescent probe imaging for visualizing multicomponent complex disease processes simultaneously (Figure 15d).[141]

7. Conclusion and outlook

NIR-II biomedical imaging is efficient for probing deeper into the tissue/body with enhanced precision as a result of the much-decreased tissue scattering and autofluorescence. With insights from materials chemistry, optics/imaging instrumentation, and medicine, development of long wavelength infrared dyes fluorescing in both the first and second NIR regions is not compromised by the adverse interactions between excitation laser and organs/tissues mentioned in this review. However, NIR dye imaging, especially with respect to NIR-II derived imaging, is still in its infant stage, calling for more high-performance syntheses with tuneable emission wavelengths and high quantum yields. Although imaging at any wavelength past 1000 nm is an improvement over the visible/infrared regions, recent work indicates that NIR-II sub-windows such as NIR-IIa and NIR-IIb provide a further boost to imaging performance, which requires NIR-II dyes with strong emission within these regions (the existing NIR-II dyes only fluoresce <1500 nm window). Adequate small molecule fluorophores with bright emission or activatable ability at this region are still lacking.[87, 116, 142, 143, 144] In addition, the polymer or supermolecular based NIR-II fluorophores are also promising due to the multi-function integration, serving as important additives for the whole library of NIR-II fluorophores.[142, 145, 146, 147]

NIR-I imaging is rapidly progressing towards a path of extensive clinical use. NIR-II imaging has reached a transformative stage, not just for basic research, but for much more. In the authors' view, a particularly important feature is that it facilitates the rapid clinical translation of the NIR-II imaging technique with the development of both fluorophore synthesis and navigation system technologies. The discovery that clinical infrared dyes display bright emission tails over 1000 nm offers exciting opportunities for enhanced surgical imaging. We anticipate that bright commercially-accessible and clinically-available NIR-II fluorescent probes will see extensive use, particularly in clinical applications when surgeons demand to assess cancer margins and map the specific anatomical structures. Integration of InGaAs camera into existing imaging navigation platforms could afford broad NIR-II spectrum imaging ability for great improving imaging quality and surgical precision. An integrated diagnostics system combining NIR imaging and other deep penetration imaging modalities will allow for more efficient detection and surgery of cancer compared to single-mode imaging. Other optical imaging modality, such as photoacoustic imaging will also improve the imaging depth in NIR-II window.[111, 142, 148, 149]

Acknowledegements

We thank Dr. Bryant C. Yung from Whiteoak Group LLC, and Swati Chandra from University of Arizona for very useful discussion and manuscript editing. This work was supported by the intramural research program of the National Institute of Biomedical Imaging and Bioengineering (NIBIB), National Institutes of Health (NIH).

Biography

Shoujun Zhu received his Ph.D. at Jilin University in 2014 under the supervision of Prof. Bai Yang and Junhu Zhang. After a two-year postdoctoral research in Hongjie Dai Lab at Stanford University, he joined National Institute of Health (NIH) in 2017 under the supervision of Prof. Xiaoyuan (Shawn) Chen. His research focuses on functional/targeting fluorophores and intravital bioimaging.

Xiaoyuan Chen received his Ph.D. in chemistry from the University of Idaho in 1999. He joined the University of Southern California as an Assistant Professor of Radiology in 2002. He then moved to Stanford University in 2004 and was promoted to Associate Professor in 2008. In the summer of 2009, he joined the Intramural Research Program of the NIBIB as a Senior Investigator and Chief of the LOMIN. He sits on the editorial board of over 10 peer-reviewed journals and is the founding editor of journal Theranostics. He is interested in developing molecular imaging modalities for better understanding of early diagnosis of disease, monitoring therapy response, and guiding drug discovery/development.

Hongjie Dai is the J. G. Jackson and C. J. Wood Professor of Chemistry at Stanford University. He obtained his bachelor’s degree in Physics from Tsinghua University, a master’s degree in Applied Sciences from Columbia University, a Ph.D. in Applied Physics/Physical Chemistry from Harvard University and performed postdoctoral research with Richard Smalley at Rice University. Dai works at the interface of chemistry, materials sciences, and biomedical sciences, with a strong interest in advancing nanoscience based infrared vision for biological imaging and detection to address fundamental and practical problems in neuroscience, cancer and cardiovascular diseases.

References

[1]. Zhang RR, Schroeder AB, Grudzinski JJ, Rosenthal EL, Warram JM, Pinchuk AN, Eliceiri KW, Kuo JS, Weichert JP, Nat. Rev. Clin. Oncol. 2017, 14, 347. [PubMed: 28094261]

[2]. Vahrmeijer AL, Hutteman M, van der Vorst JR, van de Velde CJ, Frangioni JV, Nat. Rev. Clin. Oncol. 2013, 10, 507. [PubMed: 23881033]

[3]. Mondal SB, Gao S, Zhu N, Liang R, Gruev V, Achilefu S, Adv. Cancer. Res. 2014, 124, 171. [PubMed: 25287689]

[4]. Hong G, Antaris AL, Dai H, Nat. Biomed. Eng. 2017, 1, 0010.

[5]. Stummer W, Pichlmeier U, Meinel T, Wiestler OD, Zanella F, Reulen H-J, Lancet Oncol. 2006, 7, 392. [PubMed: 16648043]

[6]. De Jesus E, Keating JJ, Kularatne SA, Jiang J, Judy R, Predina J, Nie S, Low P, Singhal S, Int. J. Mol. Imaging 2015, 2015, 469047.

[7]. Shum CF, Bahler CD, Low PS, Ratliff TL, Kheyfets SV, Natarajan JP, Sandusky GE, Sundaram CP, Endourol J. Case Rep. 2016, 2, 189.

[8]. He S, Song J, Qu J, Cheng Z, Chem. Soc. Rev. 2018, 47, 4258. [PubMed: 29725670]

[9]. Wang R, Zhang F, J. Mater. Chem. B 2014, 2, 2422.

[10]. Ding F, Zhan Y, Lu X, Sun Y, Chem. Sci. 2018, 9, 4370. [PubMed: 29896378]

[11]. Kenry Y Duan B. Liu, Adv. Mater. 2018, 1802394.

[12]. Miao Q, Pu K, Adv. Mater. 2018, e1801778.

[13]. Chen G, Zhang Y, Li C, Huang D, Wang Q, Wang Q, Adv. Healthc. Mater. 2018, e1800497.

[14]. Cai Y, Wei Z, Song C, Tang C, Han W, Dong X, Chem. Soc. Rev. 2019, 48, 22–37. [PubMed: 30444505]

[15]. Tsuboi S, Yamada S, Nakane Y, Sakata T, Yasuda H, Jin T, ECS J Solid State Sci. Technol. 2017, 7, R3093.

[16]. Hong G, Diao S, Antaris AL, Dai H, Chem. Rev. 2015, 115, 10816. [PubMed: 25997028]

[17]. Bruns OT, Bischof TS, Harris DK, Franke D, Shi Y, Riedemann L, Bartelt A, Jaworski FB, Carr JA, Rowlands CJ, Wilson MWB, Chen O, Wei H, Hwang GW, Montana DM, Coropceanu I, Achorn OB, Kloepper J, Heeren J, So PTC, Fukumura D, Jensen KF, Jain RK, Bawendi MG, Nat. Biomed. Eng. 2017, 1.

[18]. Zhu S, Herraiz S, Yue J, Zhang M, Wan H, Yang Q, Ma Z, Wang Y, He J, Antaris AL, Zhong Y, Diao S, Feng Y, Zhou Y, Yu K, Hong G, Liang Y, Hsueh AJ, Dai H, Adv. Mater. 2018, 30, e1705799.

[19]. Hong G, Diao S, Chang J, Antaris AL, Chen C, Zhang B, Zhao S, Atochin DN, Huang PL, Andreasson KI, Kuo CJ, Dai H, Nat. Photonics 2014, 8, 723. [PubMed: 27642366]

[20]. Diao S, Blackburn JL, Hong G, Antaris AL, Chang J, Wu JZ, Zhang B, Cheng K, Kuo CJ, Dai H, Angew. Chem. Int. Ed. 2015, 54, 14758–14762.

[21]. Welsher K, Liu Z, Sherlock SP, Robinson JT, Chen Z, Daranciang D, Dai H, Nat. Nanotechnol. 2009, 4, 773. [PubMed: 19893526]

[22]. Graf A, Tropf L, Zakharko Y, Zaumseil J, Gather MC, Nat. Commun. 2016, 7, 13078. [PubMed: 27721454]

[23]. Zakharko Y, Held M, Graf A, Rodlmeier T, Eckstein R, Hernandez-Sosa G, Hahnlein B, Pezoldt J, Zaumseil J, Opt. Express 2017, 25, 18092. [PubMed: 28789299]

[24]. Antaris AL, Robinson JT, Yaghi OK, Hong G, Diao S, Luong R, Dai H, ACS Nano 2013, 7, 3644. [PubMed: 23521224]

[25]. Welsher K, Sherlock SP, Dai H, Proc. Natl. Acad. Sci. U.S.A. 2011, 108, 8943. [PubMed: 21576494]

[26]. Dang X, Gu L, Qi J, Correa S, Zhang G, Belcher AM, Hammond PT, Proc. Natl. Acad. Sci. U.S.A. 2016, 113, 5179. [PubMed: 27114520]

[27]. Zhang Y, Hong G, Zhang Y, Chen G, Li F, Dai H, Wang Q, ACS Nano 2012, 6, 3695. [PubMed: 22515909]

[28]. Hong G, Robinson JT, Zhang Y, Diao S, Antaris AL, Wang Q, Dai H, Angew. Chem. 2012, 124, 9956.

[29]. Zhang Y, Zhang Y, Hong G, He W, Zhou K, Yang K, Li F, Chen G, Liu Z, Dai H, Wang Q, Biomaterials 2013, 34, 3639. [PubMed: 23415643]

[30]. Zhu CN, Jiang P, Zhang ZL, Zhu DL, Tian ZQ, Pang DW, ACS Appl. Mater. Interfaces 2013, 5, 1186. [PubMed: 23380909]

[31]. Franke D, Harris DK, Chen O, Bruns OT, Carr JA, Wilson MW, Bawendi MG, Nat. Commun. 2016, 7, 12749. [PubMed: 27834371]

[32]. He H, Lin Y, Tian ZQ, Zhu DL, Zhang ZL, Pang DW, Small 2018, 14, e1703296.

[33]. Hu F, Li C, Zhang Y, Wang M, Wu D, Wang Q, Nano Res. 2015, 8, 1637–1647.

[34]. Li C, Li F, Zhang Y, Zhang W, Zhang XE, Wang Q, ACS Nano 2015, 9, 12255. [PubMed: 26496067]

[35]. Ortgies DH, García-Villalón ÁL, Granado M, Amor S, Rodríguez EM, Santos HDA, Yao J, Rubio-Retama J, Jaque D, Nano Res. 2019, 10.1007/s12274-019-2280-4.

[36]. Wang R, Zhou L, Wang W, Li X, Zhang F, Nat. Commun. 2017, 8, 14702. [PubMed: 28281530]

[37]. Wang R, Li X, Zhou L, Zhang F, Angew. Chem. Int. Ed. 2014, 53, 12086.

[38]. Naczynski DJ, Sun C, Turkcan S, Jenkins C, Koh AL, Ikeda D, Pratx G, Xing L, Nano Lett. 2015, 15, 96. [PubMed: 25485705]

[39]. Naczynski DJ, Tan MC, Zevon M, Wall B, Kohl J, Kulesa A, Chen S, Roth CM, Riman RE, Moghe PV, Nat. Commun. 2013, 4, 2199. [PubMed: 23873342]

[40]. Zhong Y, Ma Z, Zhu S, Yue J, Zhang M, Antaris AL, Yuan J, Cui R, Wan H, Zhou Y, Wang W, Huang NF, Luo J, Hu Z, Dai H, Nat. Commun. 2017, 8, 737. [PubMed: 28963467]

[41]. Fan Y, Wang P, Lu Y, Wang R, Zhou L, Zheng X, Li X, Piper JA, Zhang F, Nat. Nanotechnol. 2018, 13, 941. [PubMed: 30082923]

[42]. Wang X, Hu H, Zhang H, Li C, An B, Dai J, Nano Res. 2017, 11, 1069.

[43]. Luo S, Zhang E, Su Y, Cheng T, Shi C, Biomaterials 2011, 32, 7127. [PubMed: 21724249]

[44]. Kosaka N, Ogawa M, Choyke PL, Kobayashi H, Future Oncol 2009, 5, 1501–1511. [PubMed: 19903075]

[45]. Zhu S, Yung BC, Chandra S, Niu G, Antaris AL, Chen X, Theranostics 2018, 8, 4141. [PubMed: 30128042]

[46]. Shang H, Fan H, Shi Q, Li S, Li Y, Zhan X, Sol. Energy Mater. Sol. Cells 2010, 94, 457.

[47]. Hilderbrand SA, Weissleder R, Curr. Opin. Chem. Biol. 2010, 14, 71. [PubMed: 19879798]

[48]. Zhang X, Bloch S, Akers W, Achilefu S, Curr. Protoc. Cytom. 2012, Chapter 12, Unit12 27.

[49]. Qi J, Fang Y, Kwok RTK, Zhang X, Hu X, Lam JWY, Ding D, Tang BZ, ACS Nano 2017, 11, 7177– [PubMed: 28692799]

[50]. Qian G, Dai B, Luo M, Yu D, Zhan J, Zhang Z, Ma D, Wang ZY, Chem. Mater. 2008, 20, 6208.

[51]. Qian G, Gao JP, Wang ZY, Chem. Commun. 2012, 48, 6426.

[52]. Qian G, Wang ZY, Chem Asian J 2010, 5, 1006. [PubMed: 20352644]

[53]. Qian G, Wang ZY, Can. J. Chem. 2010, 88, 192.

[54]. Ishizawa T, Fukushima N, Shibahara J, Masuda K, Tamura S, Aoki T, Hasegawa K, Beck Y, Fukayama M, Kokudo N, Cancer 2009, 115, 2491. [PubMed: 19326450]

[55]. Ogawa M, Kosaka N, Choyke PL, Kobayashi H, Cancer Res. 2009, 69, 1268–1272. [PubMed: 19176373]

[56]. Yi X, Wang F, Qin W, Yang X, Yuan J, Int. J. Nanomedicine 2014, 9, 1347–1365. [PubMed: 24648733]

[57]. Heo J, Lim CK, Whang DR, Shin J, Jeong SY, Park SY, Kwon IC, Kim S, Chem. Eur. J. 2012, 18, 8699. [PubMed: 22689413]

[58]. James NS, Chen Y, Joshi P, Ohulchanskyy TY, Ethirajan M, Henary M, Strekowsk L, Pandey RK, Theranostics 2013, 3, 692. [PubMed: 24019854]

[59]. Becker A, Hessenius C, Licha K, Ebert B, Sukowski U, Semmler W, Wiedenmann B, Grotzinger C, Nat. Biotechnol. 2001, 19, 327. [PubMed: 11283589]

[60]. Weissleder R, Tung CH, Mahmood U, Bogdanov A Jr., Nat. Biotechnol. 1999, 17, 375. [PubMed: 10207887]

[61]. Vinegoni C, Botnaru I, Aikawa E, Calfon MA, Iwamoto Y, Folco EJ, Ntziachristos V, Weissleder R, Libby P, Jaffer FA, Sci. Transl. Med. 2011, 3, 84ra45.

[62]. Whitley MJ, Cardona DM, Lazarides AL, Spasojevic I, Ferrer JM, Cahill J, Lee CL, Snuderl M, Blazer DG 3rd, Hwang ES, Greenup RA, Mosca PJ, Mito JK, Cuneo KC, Larrier NA, O'Reilly EK, Riedel RF, Eward WC, Strasfeld DB, Fukumura D, Jain RK, Lee WD, Griffith LG, Bawendi MG, Kirsch DG, Brigman BE, Sci. Transl. Med. 2016, 8, 320ra324.

[63]. Cosco ED, Caram JR, Bruns OT, Franke D, Day RA, Farr EP, Bawendi MG, Sletten EM, Angew. Chem. Int. Ed. 2017, 56, 13126.

[64]. Tao Z, Hong G, Shinji C, Chen C, Diao S, Antaris AL, Zhang B, Zou Y, Dai H, Angew. Chem. 2013, 125, 13240.

[65]. Tang Y, Li Y, Hu X, Zhao H, Ji Y, Chen L, Hu W, Zhang W, Li X, Lu X, Huang W, Fan Q, Adv. Mater. 2018, 30, e1801140.

[66]. Kopainsky B, Qiu P, Kaiser W, Sens B, Drexhage KH, Appl. Phys. B 1982, 29, 15.

[67]. Semonin OE, Johnson JC, Luther JM, Midgett AG, Nozik AJ, Beard MC, J. Phys. Chem. Lett. 2010, 1, 2445.

[68]. Deng G, Li S, Sun Z, Li W, Zhou L, Zhang J, Gong P, Cai L, Theranostics 2018, 8, 4116. [PubMed: 30128040]

[69]. Li B, Lu L, Zhao M, Lei Z, Zhang F, Angew. Chem. Int. Ed. 2018, 57, 7483–7487.

[70]. Chen W, Cheng C, Cosco E, Ramakrishnan S, Lingg J, Bruns O, Zink JI, Sletten E, ChemRxi 2018, 10.26434/chemrxiv.7503506.

[71]. Meng X, Zhang J, Sun Z, Zhou L, Deng G, Li S, Li W, Gong P, Cai L, Theranostics 2018, 8, 6025. [PubMed: 30613279]

[72]. Antaris AL, Chen H, Diao S, Ma Z, Zhang Z, Zhu S, Wang J, Lozano AX, Fan Q, Chew L, Zhu M, Cheng K, Hong X, Dai H, Cheng Z, Nat. Commun. 2017, 8, 15269. [PubMed: 28524850]

[73]. Zhu S, Hu Z, Tian R, Yung BC, Yang Q, Zhao S, Kiesewetter DO, Niu G, Sun H, Antaris AL, Chen X, Adv. Mater. 2018, e1802546.

[74]. Carr JA, Franke D, Caram JR, Perkinson CF, Saif M, Askoxylakis V, Datta M, Fukumura D, Jain RK, Bawendi MG, Bruns OT, Proc. Natl. Acad. Sci. U.S.A. 2018, 115, 4465. [PubMed: 29626132]

[75]. Starosolski Z, Bhavane R, Ghaghada KB, Vasudevan SA, Kaay A, Annapragada A, PLos One 2017, 12, e0187563.

[76]. Choi HS, Gibbs SL, Lee JH, Kim SH, Ashitate Y, Liu F, Hyun H, Park G, Xie Y, Bae S, Henary M, Frangioni JV, Nat. Biotechnol. 2013, 31, 148. [PubMed: 23292608]

[77]. Wang D, Lee MMS, Shan G, Kwok RTK, Lam JWY, Su H, Cai Y, Tang BZ, Adv. Mater. 2018, 30, e1802105.

[78]. Koide Y, Urano Y, Hanaoka K, Piao W, Kusakabe M, Saito N, Terai T, Okabe T, Nagano T, J. Am. Chem. Soc. 2012, 134, 5029. [PubMed: 22390359]

[79]. Yang X, Shao C, Wang R, Chu CY, Hu P, Master V, Osunkoya AO, Kim HL, Zhau HE, Chung LWK, Urol J. 2013, 189, 702.

[80]. Mayerhoffer U, Fimmel B, Wurthner F, Angew. Chem. Int. Ed. 2012, 51, 164.

[81]. Arunkumar E, Forbes CC, Noll BC, Smith BD, J. Am. Chem. Soc. 2005, 127, 3288. [PubMed: 15755140]

[82]. Gao FP, Lin YX, Li LL, Liu Y, Mayerhoffer U, Spenst P, Su JG, Li JY, Wurthner F, Wang H, Biomaterials 2014, 35, 1004. [PubMed: 24169004]

[83]. Chen J, Winter RF, Chem. Eur. J. 2012, 18, 10733. [PubMed: 22807257]

[84]. Karunakaran SC, Babu PS, Madhuri B, Marydasan B, Paul AK, Nair AS, Rao KS, Srinivasan A, Chandrashekar TK, Rao Ch M, Pillai R, Ramaiah D, ACS Chem. Biol. 2013, 8, 127. [PubMed: 23092119]

[85]. Yang E, Kirmaier C, Krayer M, Taniguchi M, Kim HJ, Diers JR, Bocian DF, Lindsey JS, Holten D, J. Phys. Chem. B 2011, 115, 10801. [PubMed: 21875047]

[86]. Azhdarinia A, Ghosh P, Ghosh S, Wilganowski N, Sevick-Muraca EM, Mol. Imaging Biol. 2012, 14, 261. [PubMed: 22160875]

[87]. Qian J, Tang BZ, Chem 2017, 3, 56.

[88]. Antaris AL, Chen H, Cheng K, Sun Y, Hong G, Qu C, Diao S, Deng Z, Hu X, Zhang B, Zhang X, Yaghi OK, Alamparambil ZR, Hong X, Cheng Z, Dai H, Nat. Mater. 2016, 15, 235. [PubMed: 26595119]

[89]. Woo SJ, Park S, Jeong JE, Hong Y, Ku M, Kim BY, Jang IH, Heo SC, Wang T, Kim KH, Yang J, Kim JH, Woo HY, ACS Appl. Mater. Interfaces 2016, 8, 15937. [PubMed: 27267787]

[90]. Ding F, Zhan Y, Lu X, Sun Y, Chem. Sci. 2018, 9, 4370. [PubMed: 29896378]

[91]. Sun Y, Ding M, Zeng X, Xiao Y, Wu H, Zhou H, Ding B, Qu C, Hou W, Er-Bu A, Zhang Y, Cheng Z, Hong X, Chem. Sci. 2017, 8, 3489. [PubMed: 28507722]

[92]. Sun Y, Qu C, Chen H, He M, Tang C, Shou K, Hong S, Yang M, Jiang Y, Ding B, Xiao Y, Xing L, Hong X, Cheng Z, Chem. Sci. 2016, 7, 6203. [PubMed: 30034761]

[93]. Zhu S, Yang Q, Antaris AL, Yue J, Ma Z, Wang H, Huang W, Wan H, Wang J, Diao S, Zhang B, Li X, Zhong Y, Yu K, Hong G, Luo J, Liang Y, Dai H, Proc. Natl. Acad. Sci. U.S.A. 2017, 114, 962. [PubMed: 28096386]

[94]. Yang Q, Ma Z, Wang H, Zhou B, Zhu S, Zhong Y, Wang J, Wan H, Antaris A, Ma R, Zhang X, Yang J, Zhang X, Sun H, Liu W, Liang Y, Dai H, Adv. Mater. 2017, 29, 1605497.

[95]. Yang Q, Hu Z, Zhu S, Ma R, Ma H, Ma Z, Wan H, Zhu T, Jiang Z, Liu W, Jiao L, Sun H, Liang Y, Dai H, J. Am. Chem. Soc. 2018, 140, 1715. [PubMed: 29337545]

[96]. Cheng K, Chen H, Jenkins CH, Zhang G, Zhao W, Zhang Z, Han F, Fung J, Yang M, Jiang Y, Xing L, Cheng Z, ACS Nano 2017, 11, 12276. [PubMed: 29202225]

[97]. Shou K, Qu C, Sun Y, Chen H, Chen S, Zhang L, Xu H, Hong X, Yu A, Cheng Z, Adv. Funct. Mater. 2017, 27, 1700995.

[98]. Zhang XD, Wang H, Antaris AL, Li L, Diao S, Ma R, Nguyen A, Hong G, Ma Z, Wang J, Zhu S, Castellano JM, Wyss-Coray T, Liang Y, Luo J, Dai H, Adv. Mater. 2016, 28, 6872. [PubMed: 27253071]

[99]. Wan H, Yue J, Zhu S, Uno T, Zhang X, Yang Q, Yu K, Hong G, Wang J, Li L, Ma Z, Gao H, Zhong Y, Su J, Antaris AL, Xia Y, Luo J, Liang Y, Dai H, Nat. Commun. 2018, 9, 1171. [PubMed: 29563581]

[100]. Wang W, Ma Z, Zhu S, Wan H, Yue J, Ma H, Ma R, Yang Q, Wang Z, Li Q, Qian Y, Yue C, Wang Y, Fan L, Zhong Y, Zhou Y, Gao H, Ruan J, Hu Z, Liang Y, Dai H, Adv. Mater. 2018, 30, e1800106.

[101]. Wan H, Ma H, Zhu S, Wang F, Tian Y, Ma R, Yang Q, Hu Z, Zhu T, Wang W, Ma Z, Zhang M, Zhong Y, Sun H, Liang Y, Dai H, Adv. Funct. Mater. 2018, 28, 1804956.

[102]. Tian R, Ma H, Yang Q, Wan H, Zhu S, Chandra S, Sun H, Kiesewetter DO, Niu G, Liang Y, Chen X, Chem. Sci. 2019, 10, 326. [PubMed: 30713641]

[103]. Gao RW, Teraphongphom N, de Boer E, van den Berg NS, Divi V, Kaplan MJ, Oberhelman NJ, Hong SS, Capes E, Colevas AD, Warram JM, Rosenthal EL, Theranostics 2018, 8, 2488. [PubMed: 29721094]

[104]. Li D, Zhang J, Chi C, Xiao X, Wang J, Lang L, Ali I, Niu G, Zhang L, Tian J, Ji N, Zhu Z, Chen X, Theranostics 2018, 8, 2508. [PubMed: 29721096]

[105]. Qi J, Sun C, Zebibula A, Zhang H, Kwok RTK, Zhao X, Xi W, Lam JWY, Qian J, Tang BZ, Adv. Mater. 2018, 30, e1706856.

[106]. Xu G, Yan Q, Lv X, Zhu Y, Xin K, Shi B, Wang R, Chen J, Gao W, Shi P, Fan C, Zhao C, Tian H, Angew. Chem. Int. Ed. 2018, 57, 3626.

[107]. Kang H, Gravier J, Bao K, Wada H, Lee JH, Baek Y, El Fakhri G, Gioux S, Rubin BP, Coll JL, Choi HS, Adv. Mater. 2016, 28, 8162. [PubMed: 27414255]

[108]. Sheng Z, Hu D, Zheng M, Zhao P, Liu H, Gao D, Gong P, Gao G, Zhang P, Ma Y, Cai L, ACS Nano 2014, 8, 12310. [PubMed: 25454579]

[109]. Chen Q, Liang C, Wang C, Liu Z, Adv. Mater. 2015, 27, 903. [PubMed: 25504416]

[110]. Wu W, Mao D, Hu F, Xu S, Chen C, Zhang CJ, Cheng X, Yuan Y, Ding D, Kong D, Liu B, Adv. Mater. 2017, 29, 1700548.

[111]. Guo B, Sheng Z, Hu D, Liu C, Zheng H, Liu B, Adv. Mater. 2018, e1802591.

[112]. Sasaki S, Drummen GPC, Konishi G.-i, J. Mater. Chem. C 2016, 4, 2731.

[113]. Sun H, Zhong C, Bredas JL, Chem J. Theory Comput. 2015, 11, 3851.

[114]. Wang Y, Wang J, Ma Q, Li Z, Yuan Q, Nano Res. 2018, 11, 5499.

[115]. Ma Z, Wan H, Wang W, Zhang X, Uno T, Yang Q, Yue J, Gao H, Zhong Y, Tian Y, Sun Q, Liang Y, Dai H, Nano Res. 2018, 12, 273.

[116]. Miao Q, Xie C, Zhen X, Lyu Y, Duan H, Liu X, Jokerst JV, Pu K, Nat. Biotechnol. 2017, 35, 1102. [PubMed: 29035373]

[117]. Chen W, Wang G, Yung BC, Liu G, Qian Z, Chen X, ACS Nano 2017, 11, 5062. [PubMed: 28437610]

[118]. Feng Y, Zhu S, Antaris AL, Chen H, Xiao Y, Lu X, Jiang L, Diao S, Yu K, Wang Y, Herraiz S, Yue J, Hong X, Hong G, Cheng Z, Dai H, Hsueh AJ, Chem. Sci. 2017, 8, 3703. [PubMed: 28626555]

[119]. Hagenbuch B, Clin. Pharmacol. Ther. 2010, 87, 39. [PubMed: 19924123]

[120]. Cilliers C, Nessler I, Christodolu N, Thurber GM, Mol. Pharm. 2017, 14, 1623. [PubMed: 28294622]

[121]. Williams DF, Biomaterials 2008, 29, 2941. [PubMed: 18440630]

[122]. Ratner BD, J. Cardiovasc. Transl. Res. 2011, 4, 523. [PubMed: 21710333]

[123]. Yu M, Liu J, Ning X, Zheng J, Angew. Chem. Int. Ed. 2015, 54, 15434.

[124]. Pham W, Medarova Z, Moore A, Bioconjug. Chem. 2005, 16, 735. [PubMed: 15898745]

[125]. Yang H, Mao H, Wan Z, Zhu A, Guo M, Li Y, Li X, Wan J, Yang X, Shuai X, Chen H, Biomaterials 2013, 34, 9124. [PubMed: 24008037]

[126]. Eser S, Messer M, Eser P, von Werder A, Seidler B, Bajbouj M, Vogelmann R, Meining A, von Burstin J, Algul H, Pagel P, Schnieke AE, Esposito I, Schmid RM, Schneider G, Saur D, Proc. Natl. Acad. Sci. U.S.A. 2011, 108, 9945. [PubMed: 21628592]

[127]. Grossi M, Morgunova M, Cheung S, Scholz D, Conroy E, Terrile M, Panarella A, Simpson JC, Gallagher WM, O'Shea DF, Nat. Commun. 2016, 7, 10855. [PubMed: 26927507]

[128]. Rosenthal EL, Warram JM, de Boer E, Chung TK, Korb ML, Brandwein-Gensler M, Strong TV, Schmalbach CE, Morlandt AB, Agarwal G, Hartman YE, Carroll WR, Richman JS, Clemons LK, Nabell LM, Zinn KR, Clin. Cancer Res. 2015, 21, 3658. [PubMed: 25904751]

[129]. Jafari MD, Wexner SD, Martz JE, McLemore EC, Margolin DA, Sherwinter DA, Lee SW, Senagore AJ, Phelan MJ, Stamos MJ, J. Am. Coll. Surg. 2015, 220, 82. [PubMed: 25451666]

[130]. Vlek SL, van Dam DA, Rubinstein SM, de Lange-de Klerk ESM, Schoonmade LJ, Tuynman JB, Meijerink W, Ankersmit M, Surg. Endosc. 2017, 31, 2731. [PubMed: 27844236]

[131]. Abu-Rustum NR, J. Natl. Compr. Canc. Netw. 2014, 12, 288. [PubMed: 24586087]

[132]. van der Vorst JR, Schaafsma BE, Hutteman M, Verbeek FP, Liefers GJ, Hartgrink HH, Smit VT, Lowik CW, van de Velde CJ, Frangioni JV, Vahrmeijer AL, Cancer 2013, 119, 3411. [PubMed: 23794086]

[133]. Yang W, Yuste R, Nat. Methods 2017, 14, 349. [PubMed: 28362436]

[134]. Wang F, Wan H, Yue J, Zhang M, Ma Z, Sun Q, Qu L, Ma H, Zhong Y, Tian Y, Hong G, Li WJ, Liang Y, Liu L, Dai H, BioRxiv 2018, 10.1101/447433.

[135]. Del Bonis-O'Donnell JT, Chio L, Dorlhiac GF, McFarlane IR, Landry MP, Nano Res. 2018, 11, 5144. [PubMed: 31105899]

[136]. Vinegoni C, Feruglio PF, Gryczynski I, Mazitschek R, Weissleder R, Adv. Drug Deliv. Rev. 2018, 10.1016/j.addr.2018.01.019.

[137]. Arlauckas SP, Garris CS, Kohler RH, Kitaoka M, Cuccarese MF, Yang KS, Miller MA, Carlson JC, Freeman GJ, Anthony RM, Weissleder R, Pittet MJ, Sci. Transl. Med. 2017, 9.

[138]. Pittet MJ, Weissleder R, Cell 2011, 147, 983. [PubMed: 22118457]

[139]. Entenberg D, Rodriguez-Tirado C, Kato Y, Kitamura T, Pollard JW, Condeelis J, Intravital 2015, 4, e1086613.

[140]. Chi C, Du Y, Ye J, Kou D, Qiu J, Wang J, Tian J, Chen X, Theranostics 2014, 4, 1072. [PubMed: 25250092]

[141]. Hu S, Kang H, Baek Y, El Fakhri G, Kuang A, Choi HS, Adv. Healthc. Mater. 2018, e1800066.

[142]. Jiang Y, Upputuri PK, Xie C, Lyu Y, Zhang L, Xiong Q, Pramanik M, Pu K, Nano Lett. 2017, 17, 4964. [PubMed: 28654292]

[143]. Zhen X, Tao Y, An Z, Chen P, Xu C, Chen R, Huang W, Pu K, Adv. Mater. 2017, 29, 1606665.

[144]. Zhen X, Xie C, Pu K, Angew. Chem. Int. Ed. 2018, 57, 3938.

[145]. Lu X, Yuan P, Zhang W, Wu Q, Wang X, Zhao M, Sun P, Huang W, Fan Q, Polym. Chem. 2018, 9, 3118.

[146]. Shou K, Tang Y, Chen H, Chen S, Zhang L, Zhang A, Fan Q, Yu A, Cheng Z, Chem. Sci. 2018, 9, 3105. [PubMed: 29732093]

[147]. Guo B, Sheng Z, Kenry K, Hu D, Lin X, Xu S, Liu C, Zheng H, Liu B, Mater. Horiz. 2017, 4, 1151.

[148]. Li J, Pu K, Chem. Soc. Rev. 2019, 48, 38. [PubMed: 30387803]

[149]. Chen Q, Chen J, Yang Z, Zhang L, Dong Z, Liu Z, Nano Res. 2018, 11, 5657.

[150]. Smith AM, Mancini MC, Nie S, Nat. Nanotechnol. 2009, 4, 710. [PubMed: 19898521]

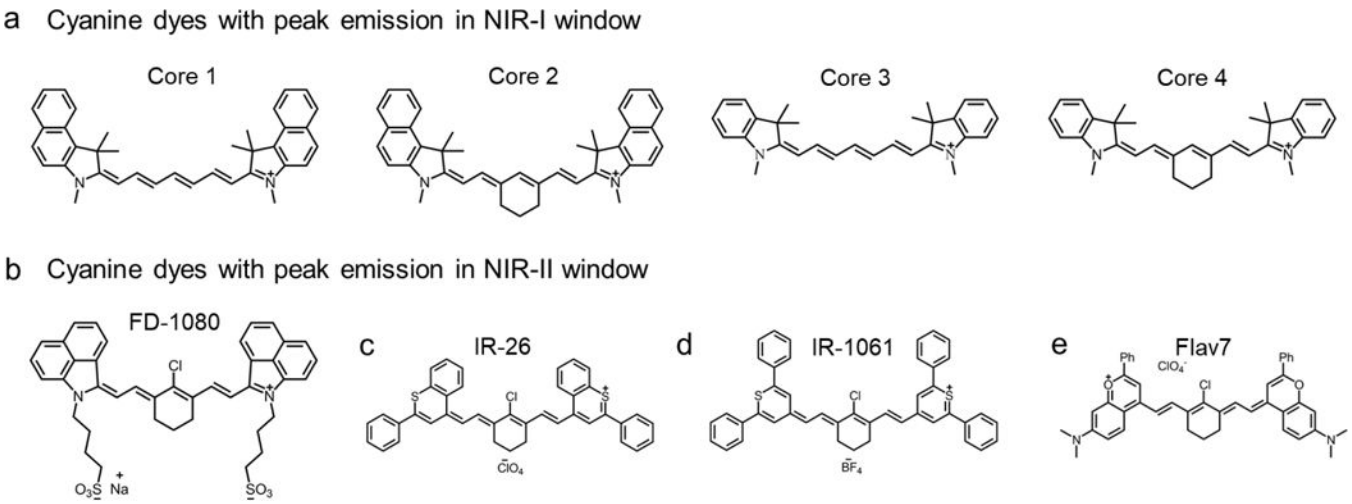

Figure 1. Typical chemical structures of cyanine and other polymethine fluorophores in NIR-I/II windows.

a) The typical backbone structure of cyanine dyes. Representativeness of Core 1 is ICG, IR-125; Core 2: IR-820, IR-830, Cy7.5; Core 3: DiR, HITCI; Core 4: IRDye800cw, IR-783, IR12-N3, Cy7, IR-775, IR-780, etc. The cyclohexene can also be replaced by cyclopentene or other derivatives, e.g. IR-806, IR-797, IR-140, etc. NIR-II tail emission of part of NIR-I dyes was observed.[73] Reprinted with permission from Ref. [73]. b) Chemical structure of FD1080,[69] similar core structure also includes commercial IR-1048 and synthesized IR-1048-MZ.[71] c) Chemical structure of IR-26 dye. d) Chemical structure of IR-1061. e) Flav7 absorbs and emits light over 1000 nm, with much-enhanced QY and absorption coefficient. Reprinted with permission from Ref. [63].

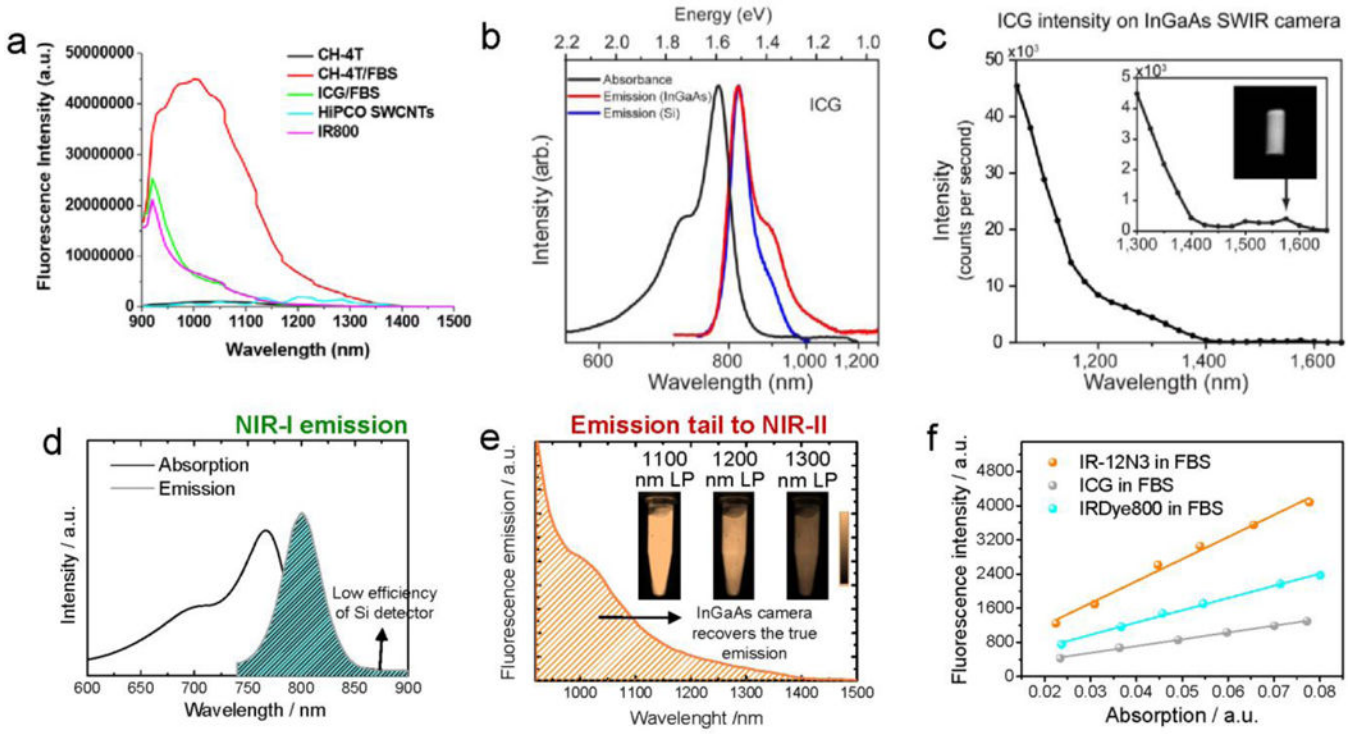

Figure 2. Highly photoluminescent cyanine dyes (peak emission at 750–850 nm) have nonnegligible emission tails ending up to NIR-II region.

a) The NIR-II tail of ICG and IRDye800 was first reported by Antaris et al.[72] in their paper Figure S14: NIR-II spectra of NIR-I/II dyes past 1000 nm. Emission spectra at wavelengths longer than 900 nm after 808 nm laser excitation from NIR-II fluorophores including CH-4T, CH-4T/FBS, and HiPCO carbon nanotubes as well as NIR-I dyes such as IRDye800 and ICG/FBS. Reprinted with permission from Ref. [72]. b-c) NIR-II fluorescence emission of typical cyanine dye, ICG. b) Silicon detector (blue line) artificially suppressed the true emission shoulder due to the sharp drop in quantum efficiency starting at 900 nm. The InGaAs detector (red line) can recover the true emission tail of ICG. c) The NIR-II fluorescence of ICG was even detectable up to 1575 nm. Reprinted with permission from Ref. [74]. d-f) Absorption, NIR-I and NIR-II emission of commercial cyanine dye IR-12N3. The inset figure is 2D NIR-II imaging of IR-12N3 aqueous solution at 1100, 1200 and 1300 sub-window, respectively. d) Testing the emission of IR-12N3 under a silicon detector recorded a false emission spectrum, which disobeyed the mirror rule (absorption spectrum is symmetry with the emission spectrum). e) The InGaAs 1D detector with high sensitivity spanning from 850 to >2000 nm can monitor the accurate emission spectrum of IR-12N3 in this region. f) NIR-I QYs of IR-12N3 was quantified 2–3 fold higher than IRDye800CW or ICG in FBS buffers. Reprinted with permission from Ref. [73].

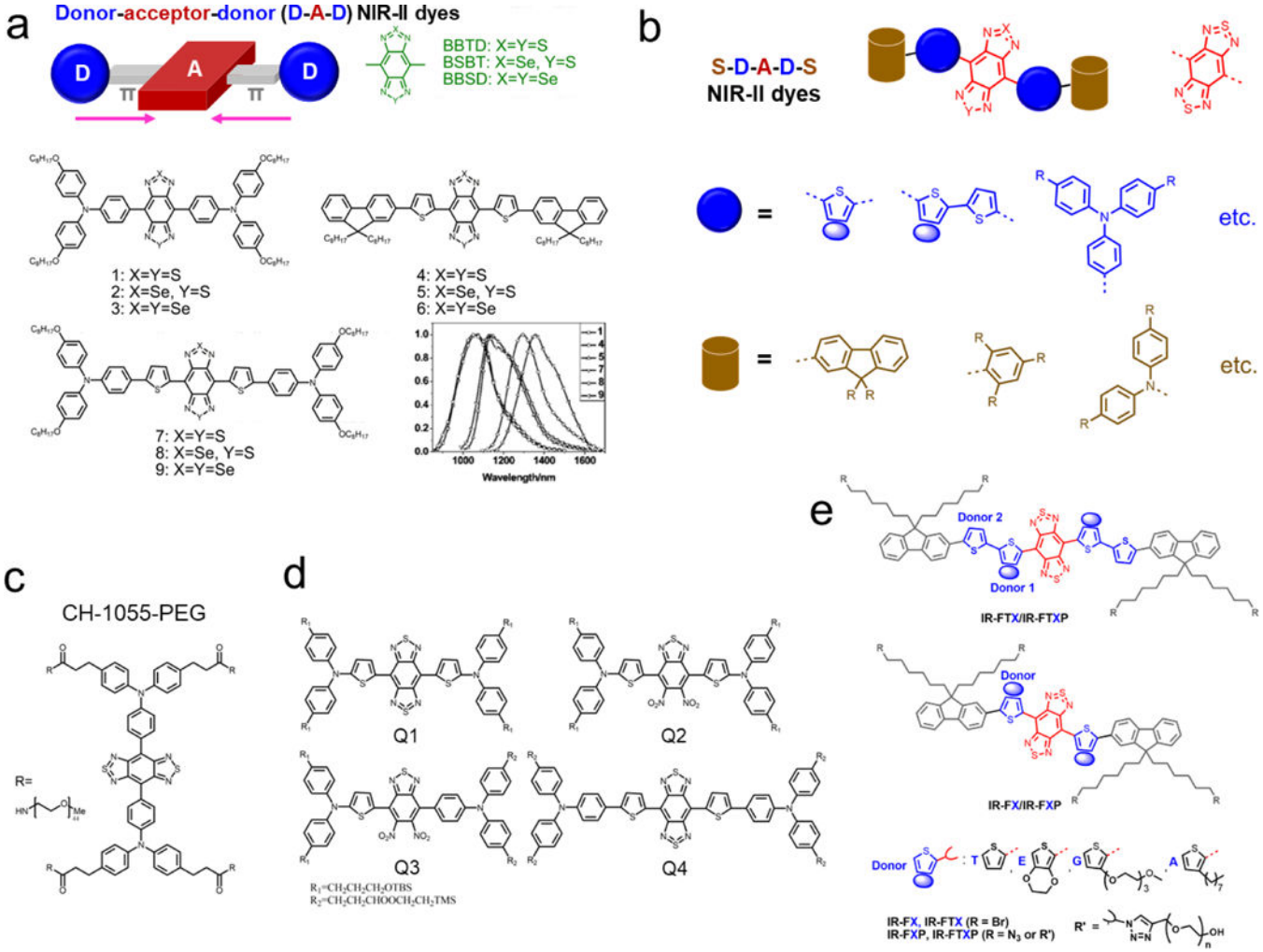

Figure 3. Chemical structures of current hydrophobic and water-soluble D-A-D fluorophores.

a) Peak regulation (from 1000 to 1400 nm) of hydrophobic D-A-D dyes with tuning both acceptors and donors. A typical guidance of chemical structure design is reported for D-A-D fluorophores with three acceptors, and the selective combination produced fluorophores 1–9 with tunable emission spectra in toluene. Reprinted with permission from Ref. [50][51]. b) The general structure of recently reported D-A-D/S-D-A-D-S dyes for NIR-II bioimaging. c) The first water-soluble NIR-II dye is CH1055-PEG. Reprinted with permission from Ref. [88]. d) Design of NIR-II dyes based on CH1055 scaffold and the chemical structures of Q1-Q4. Reprinted with permission from Ref. [92]. e) Schematic illustration of the design of bright molecular fluorophores with either single or double-donor optimization produced several key fluorophores.[18, 89, 93, 94] Reprinted with permission from Ref. [95]. To avoid repetition, please also check other structures in Figure 6,[72] 8[98, 101, 102], 10.[91] and Table 1.

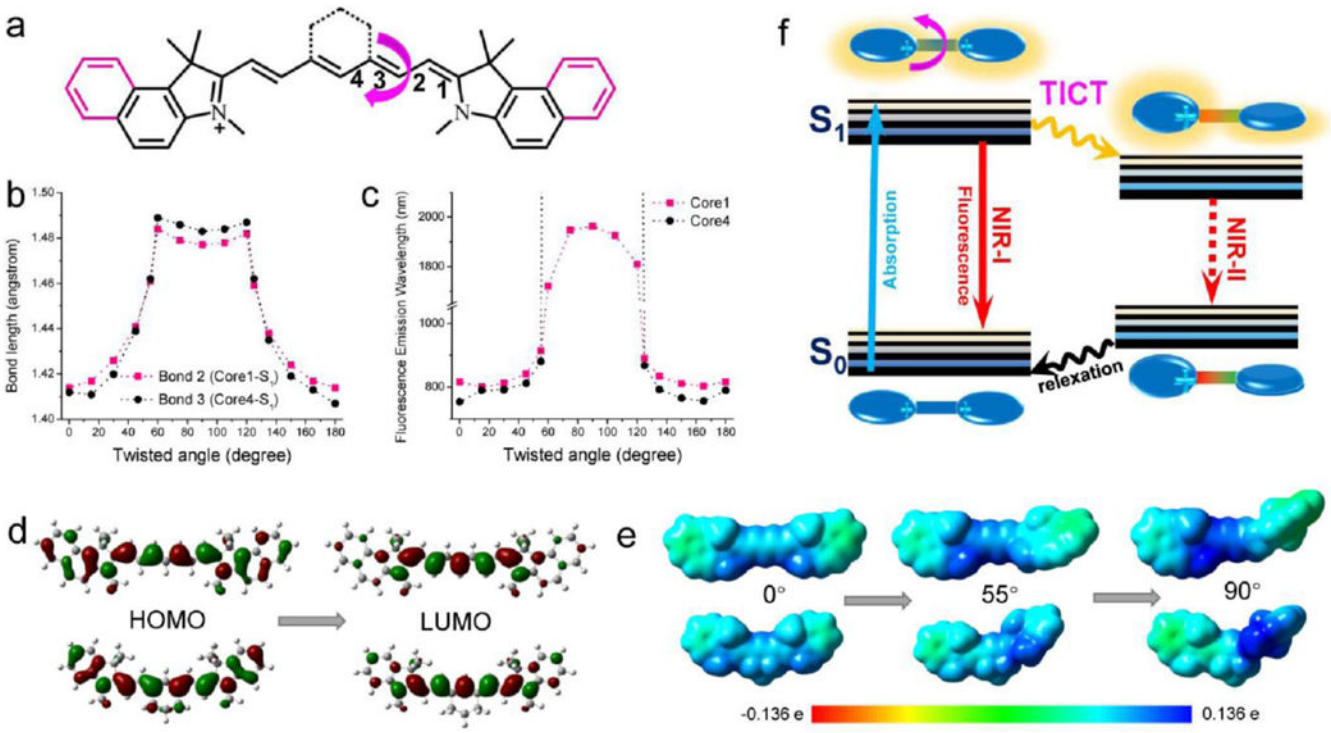

Figure 4. Theoretical calculation revealed the NIR-II tail emission mechanism of cyanine dyes.

a) The calculated backbone structure of ICG and IR-12N3. b-c) The relationship between bond lengths and emission wavelength with respect to twisted angles. d) The simulated HOMOs and LUMOs shapes for two typical cyanine core structures. e) Quantitatively mapping of electrostatic potential (ESP) exterior for the backbone of cyanine dyes. f) The graphic interpretation of the emission tail mechanism and TICT was suggested for such tail emission behaviors. Reprinted with permission from Ref. [73].

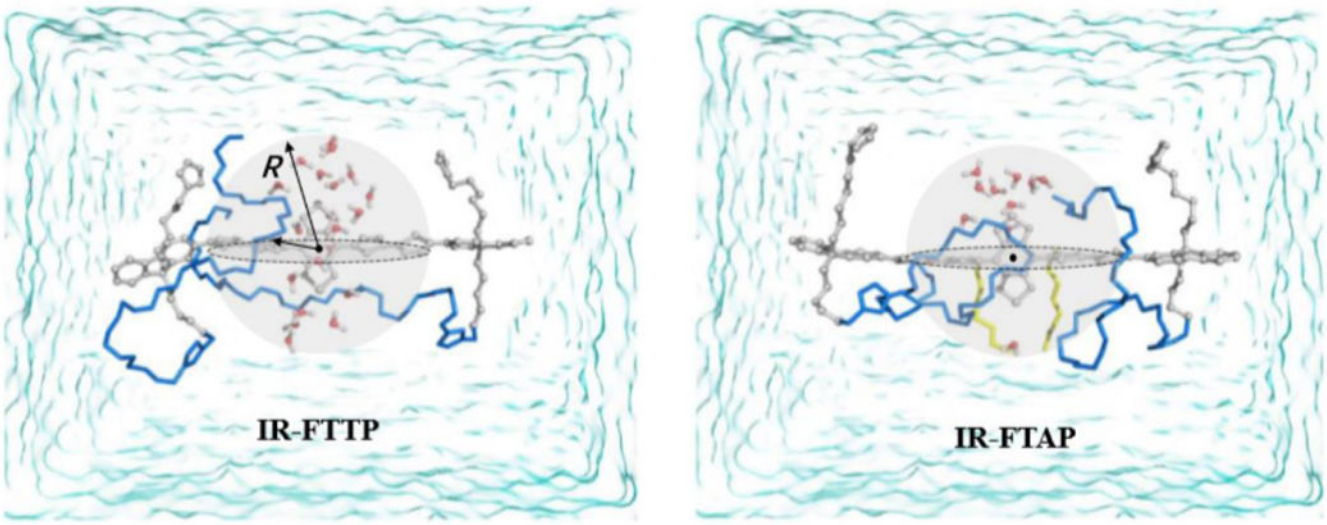

Figure 5. Theoretical simulation of the interaction between H_2O molecules and the BBTD core acceptor of the D-A-D dyes (IR-FTAP and IR-FTTP).

Grey part indicates the π-electron cloud; blue line represents a PEG chain; the yellow line shows an alkyl chain; the H_2O molecules neighboring the BBTD internal in the adequate contact space (R = 6 ~ 7 Å) are shown as a definite water model. Reprinted with permission from Ref. [95].

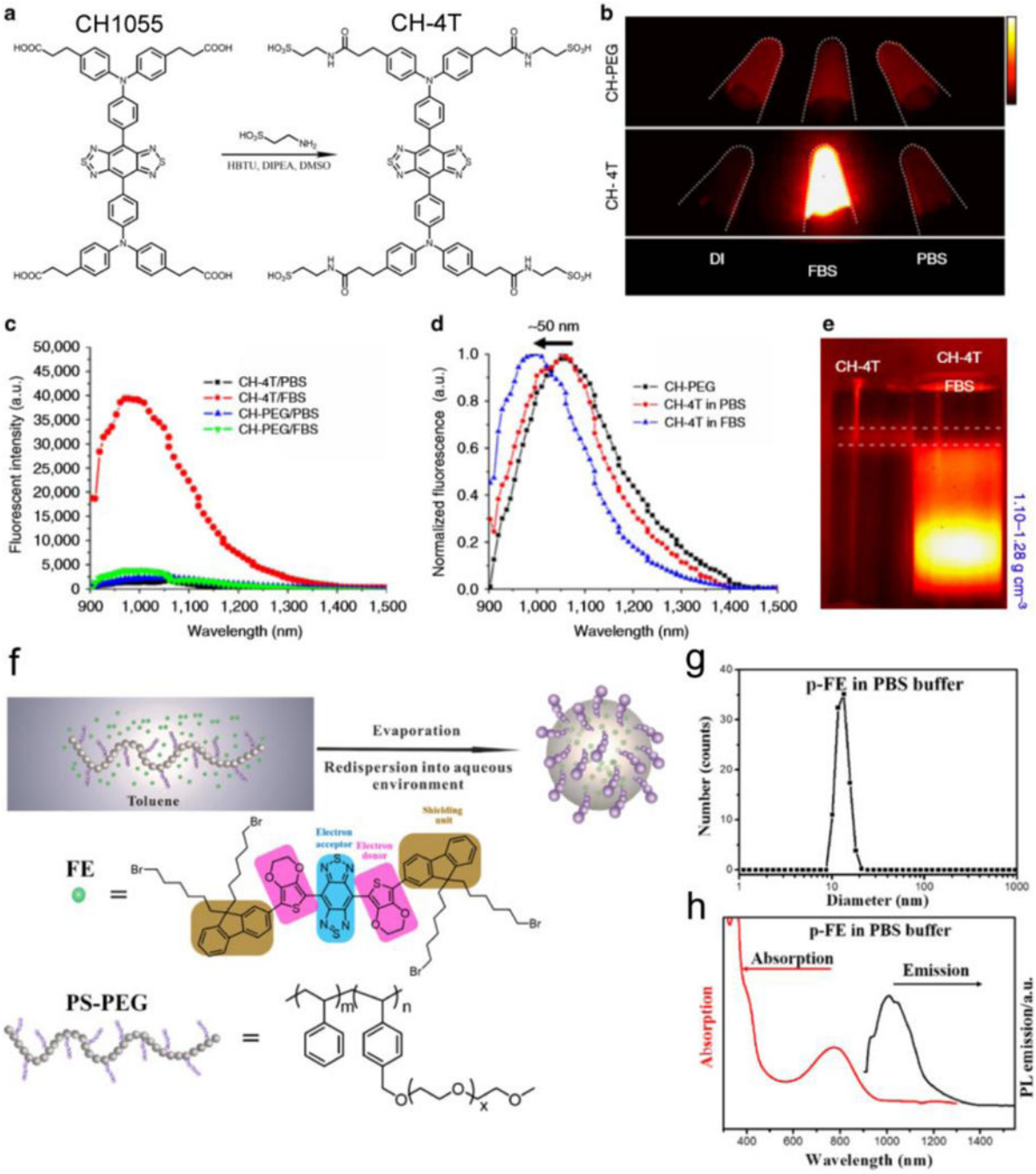

Figure 6. QYs enhancement of NIR-II fluorophores.

a) CH1055 and its derivative CH-4T. b) NIR-II imaging of CH-PEG and CH-4T in DIUF, FBS and PBS, respectively (imaging details: 1100 nm long-pass filter (LP), 10 ms exposure time). c) NIR-II emission spectra of CH-PEG and CH-4T. d) Intensity normalized fluorescent spectra of CH-4T in a different medium, indicating a blue shift in FBS. e) DGU proved that CH-4T@FBS complex has a larger weight than free CH-4T molecules (imaging details: 1000 nm LP, 10 ms). Reprinted with permission from Ref. [72]. f-h) The bright NIR-II nanocomplex p-FE was developed by polymer wrapping method. f) Scheme of synthesis

of the p-FE fluorophore. g-h) DLS analysis, absorption, and NIR-II emission spectra (808 nm laser excitation) of the p-FE fluorophore in PBS buffer. Reprinted with permission from Ref. [99].

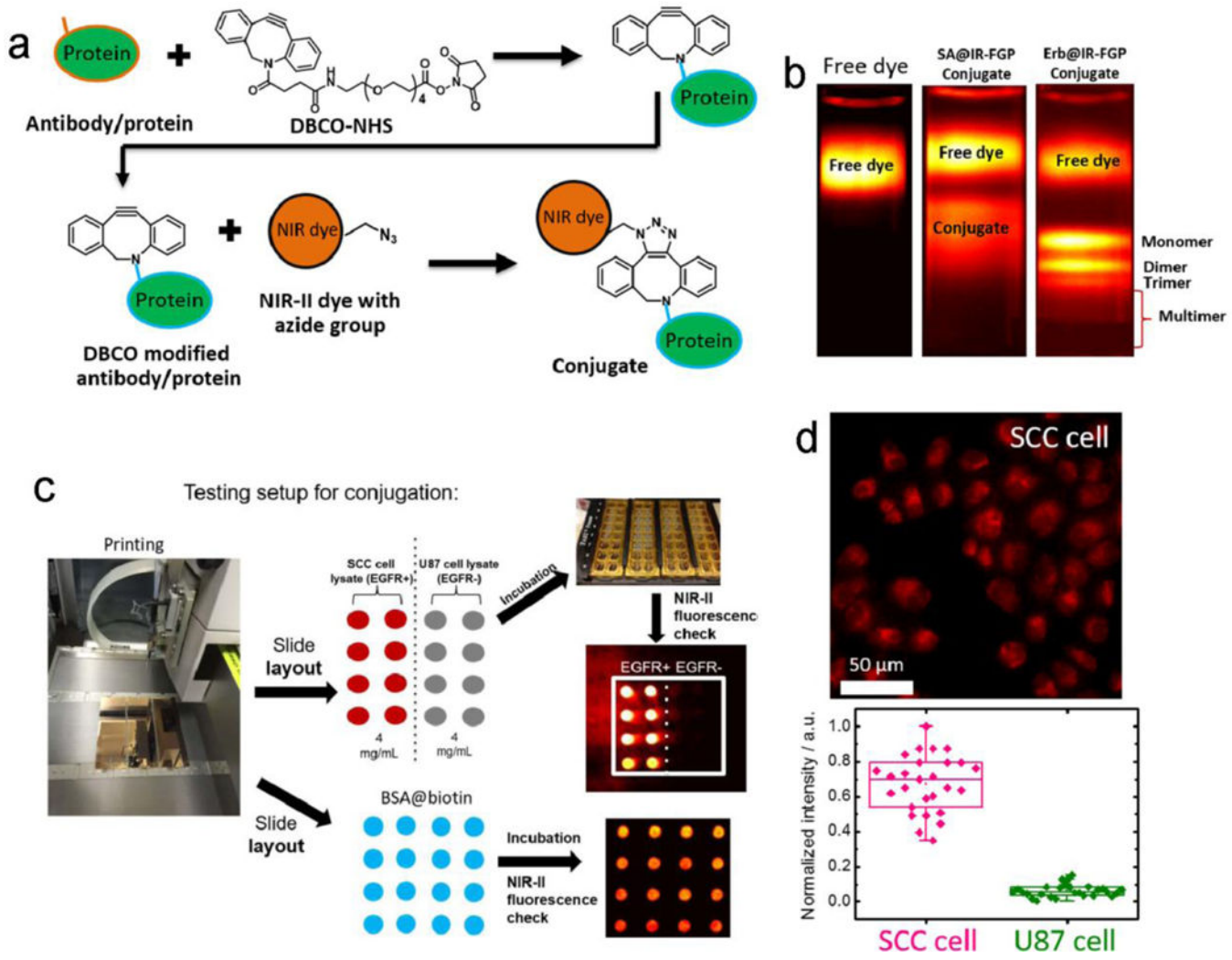

Figure 7. Bioconjugations between NIR-II fluorophores and proteins.

a) The copper-free click chemistry was applied to conjugate the IR-FGP fluorophore with proteins of interest. b) Density gradient ultracentrifugation (DGU) was performed to purify the SA@IR-FGP and Erb@IR-FGP conjugates. The applied sucrose gradient encompasses from 1.06–1.23 g/ cm^3 (15–50 wt.%) (imaging details: 850/1000 nm short-pass (SP) filters and 900/1100-nm LP emission filters). c) A new reverse phase protein lysate microarray method was exploited to test the quality of conjugates. In detail, 1. The BSA-biotin, "catching" a primary antibody or cell lysate, was printed on the gold chips. 2. The purified conjugates were incubated on top of the printed spots under the cavity of frames. 3. Check the PL intensity by 10X magnification NIR II set-up with desired long-pass emission filter combination. d) Targeted cell imaging by Erb@IR-FGP on positive and negative cell lines respectively (imaging details: 785 nm excitation and 1050 nm LP emission filter). Reprinted with permission from Ref. [93].

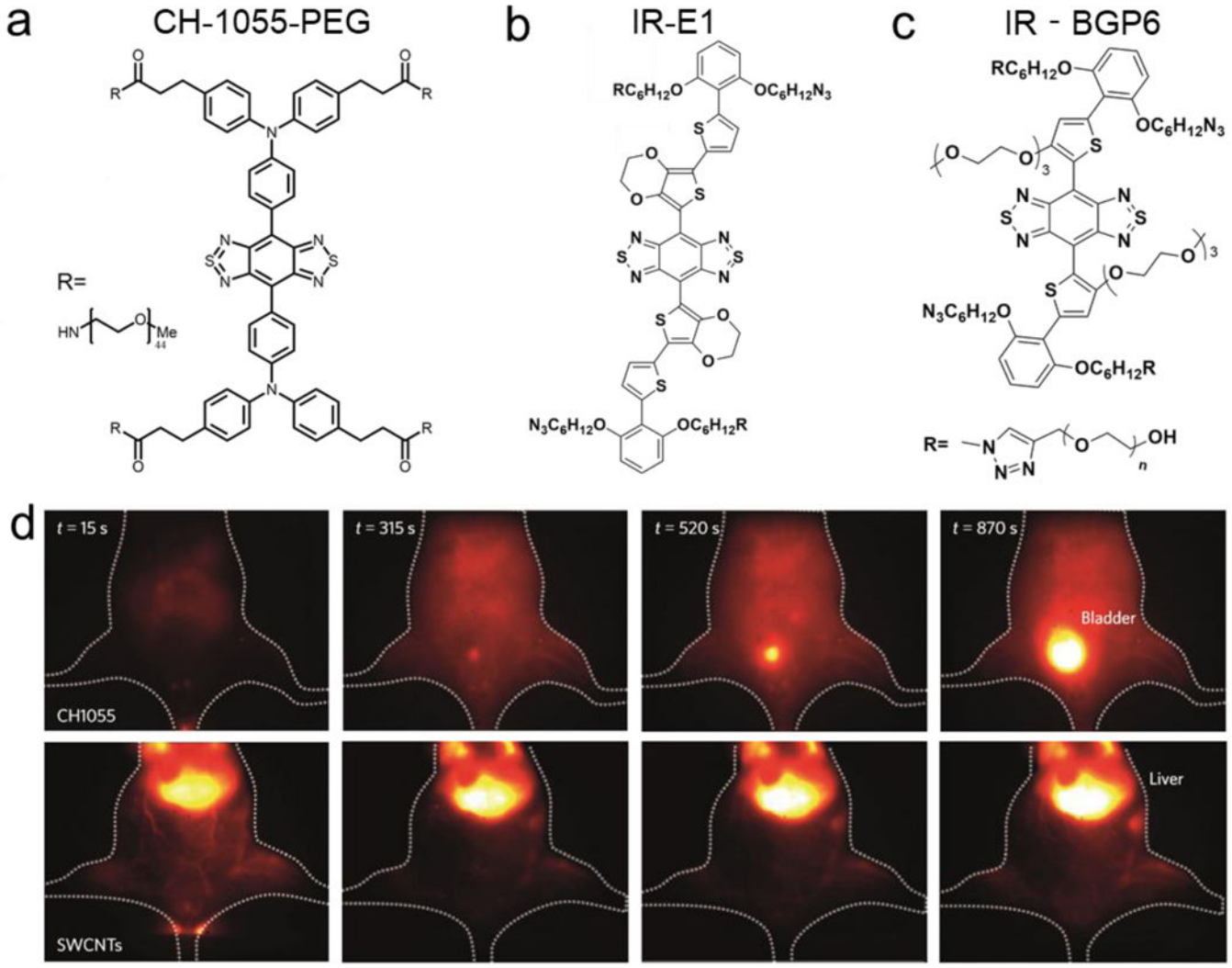

Figure 8. Renally excreted NIR-II dyes.

a-c) Chemical structure of renally excreted NIR-II dyes (CH1055PEG,[88] IR-E1,[98] and IR-BGP6[100, 101]) with D-A-D or S-D-A-D-S structures. d) Injection of CH1055-PEG and HiPCO SWCNTs fluorophores in mouse showed disparate liver and bladder signals, respectively, indicating the typical behavior of renally excreted molecules (imaging details: 1200 nm LP, 100 ms). Reprinted with permission from Ref. [88].

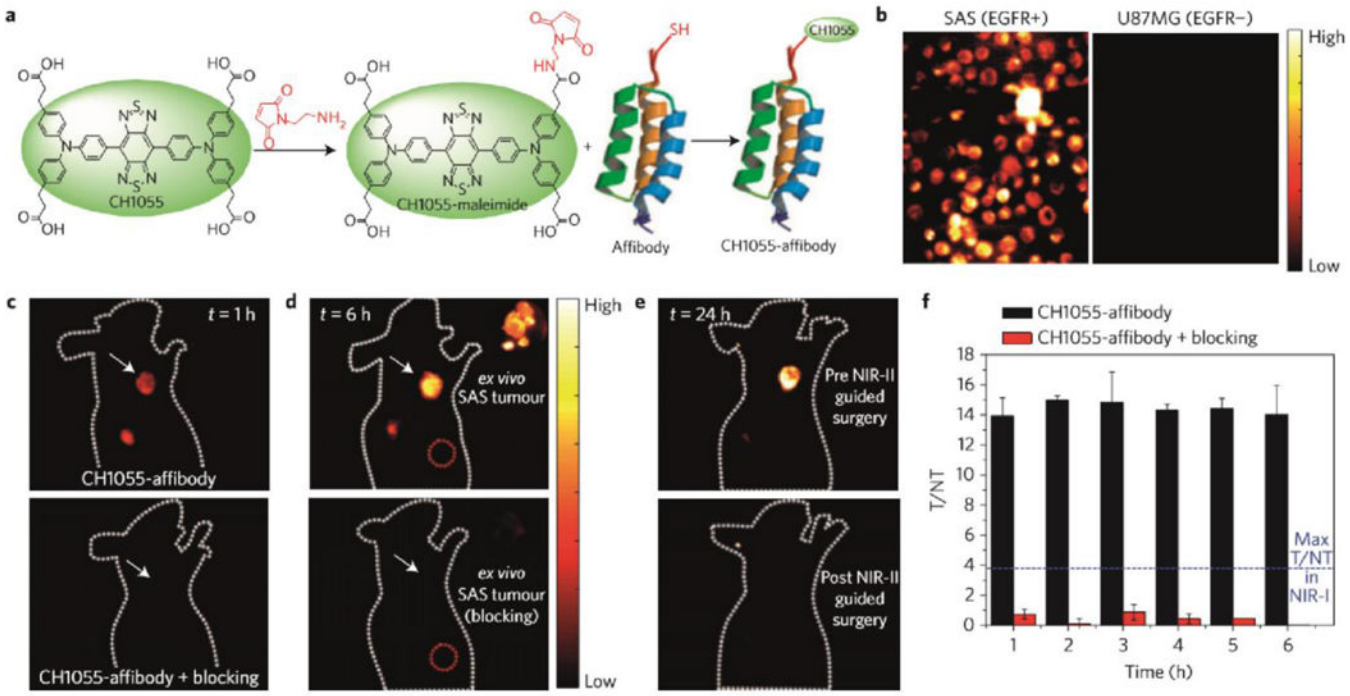

Figure 9. The first NIR-II molecular imaging-guided tumor surgery.

a) Reaction scheme of NIR-II conjugate CH1055@affibody. b) Targeted cell staining indicated the successful conjugation of CH1055 with EGFR affibody. c-d) NIR-II imaging with tail injection of CH1055@affibody conjugate showed great targeting ability. e) The imaging-guided surgery can remove the tumor via complete excision. f) T/NT ratios with CH1055-affibody targeted tumor imaging. Reprinted with permission from Ref. [88].

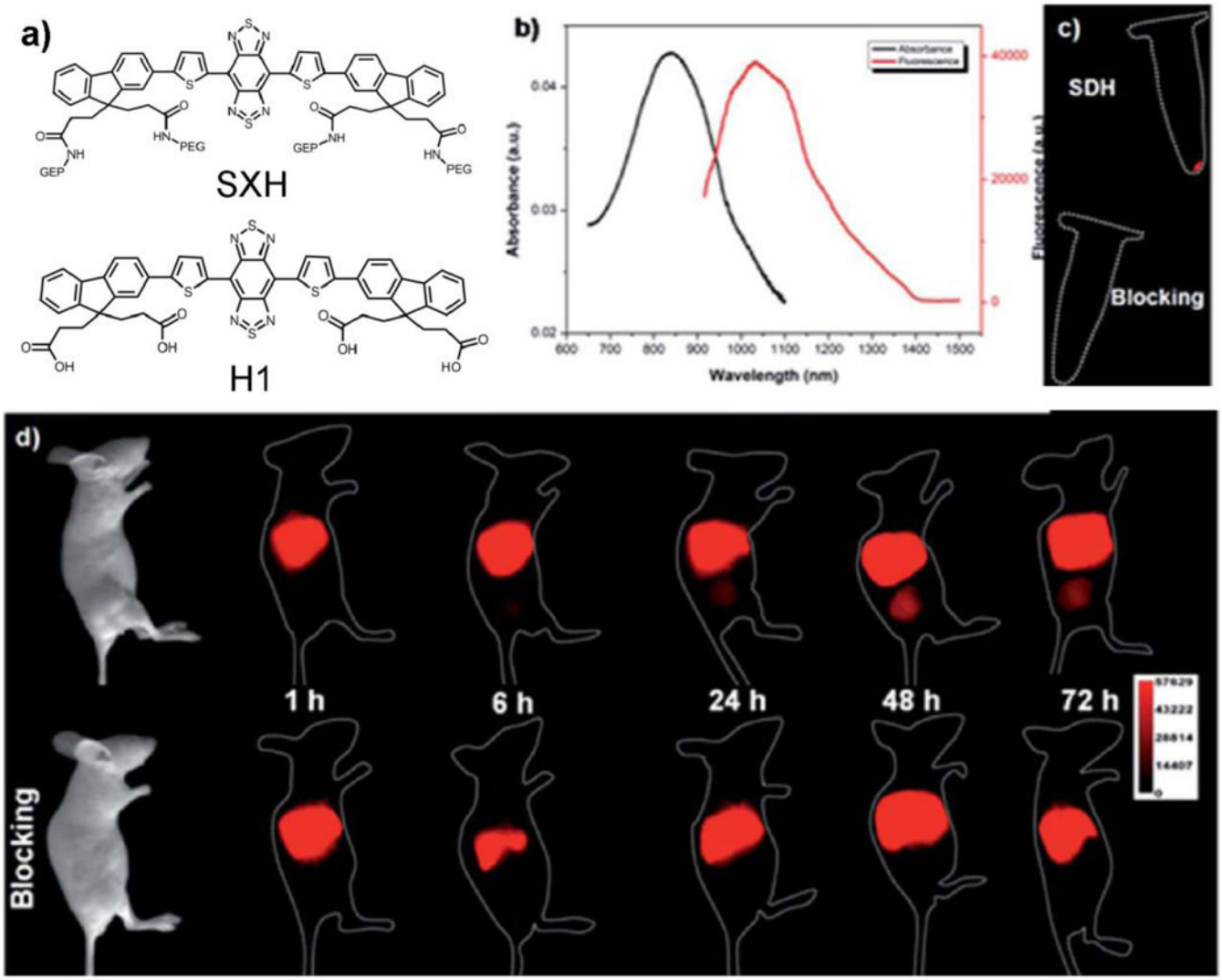

Figure 10. NIR-II molecular imaging with the peptide conjugate.

a) Scheme of SXH and H1. b) Absorption and emission of H1. c) U87MG cell targeted imaging with H1@RGD conjugates. d) U87MG tumor-bearing mice imaging with H1@RGD conjugates or the blocking agent RGD (imaging details: 1000 nm LP, 200 ms). Reprinted with permission from Ref. [91].

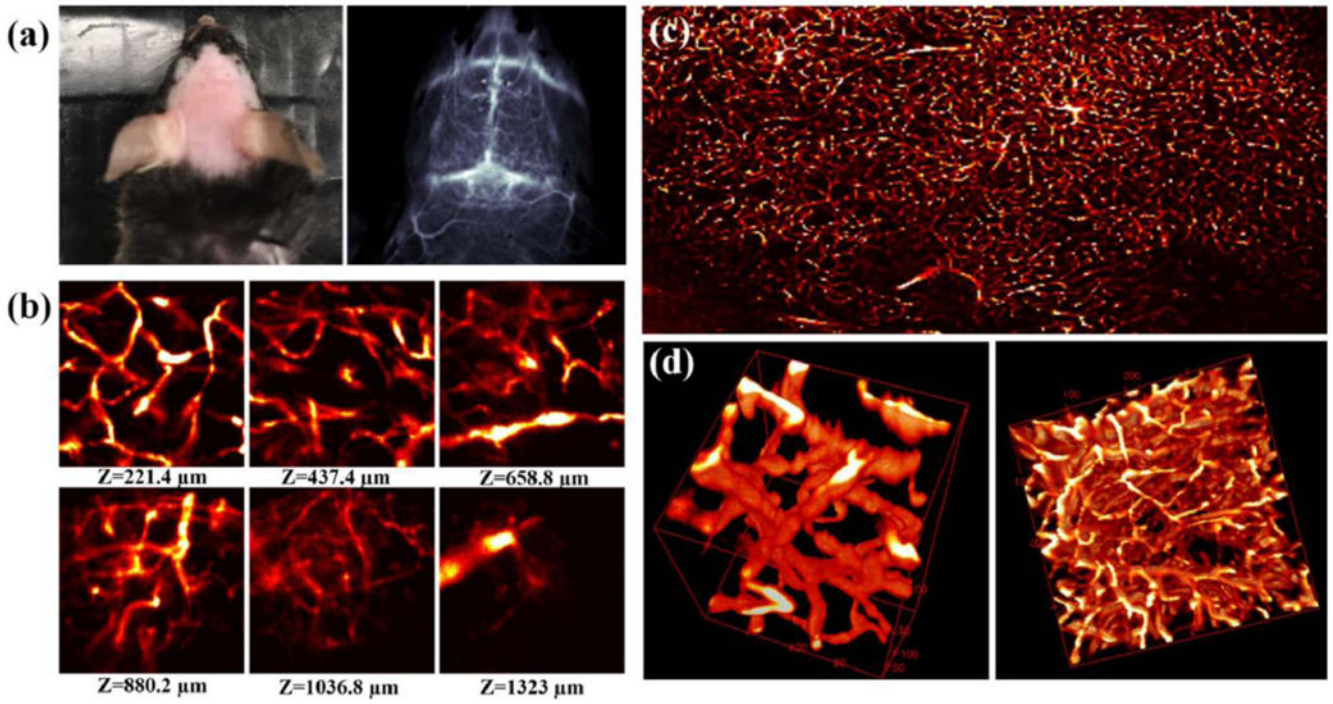

Figure 11. NIR-II confocal imaging of brain vessel.

a) Picture and NIR-II imaging of mouse brain after p-FE administration above 1200 nm long pass filter and 5 ms exposure time. b-d) NIR-II confocal imaging can reconstruct the three-dimensional vessel structure in the mouse brain. The field view of b is 200 μm^2, c is 3000*2000 μm (imaging details: 785 nm excitation, 1100 nm LP emission, laser power ~30 mW). Reprinted with permission from Ref. [99].

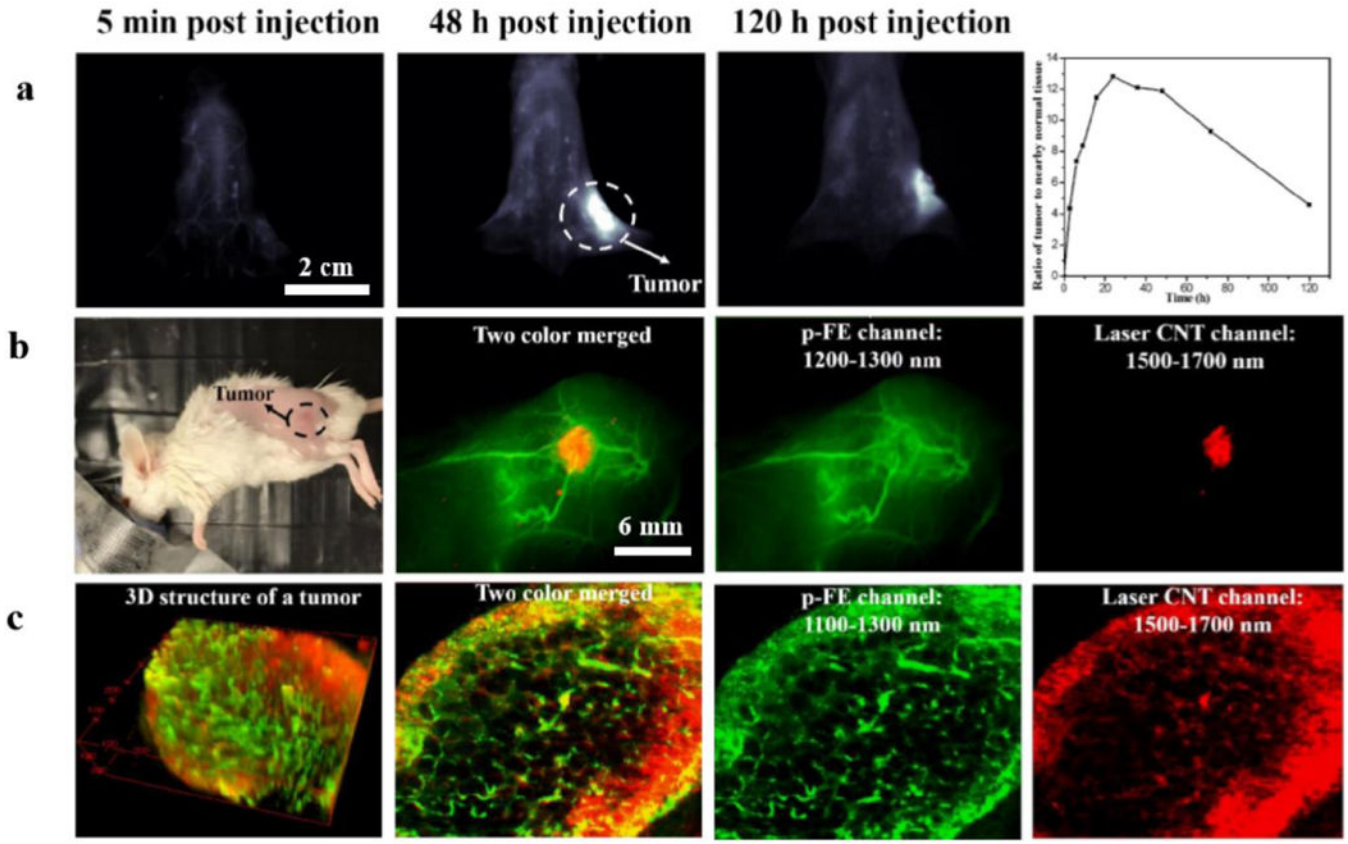

Figure 12. NIR-II dual-color tumor imaging.

a) Whole body imaging of 4T1 tumor-bearing mouse after p-FE administration (imaging details: 1300 nm LP, 5 ms). b) The laser-ablation CNT was used to light up the 4T1 tumor while p-FE was injected to visualize the tumor vessels. c) NIR-II confocal dual-color imaging of 4T1 tumor. The field view is 740 μm^2, and the scanned depth was 220 μm (imaging details: 2–5.4 μm step size, Laser power ~30 mW, 15 min/frame, Pinhole: 150–300 μm, 1100 nm LP+1300 nm SP for p-FE, 1500 nm LP for laser CNT). Reprinted with permission from Ref. [99].

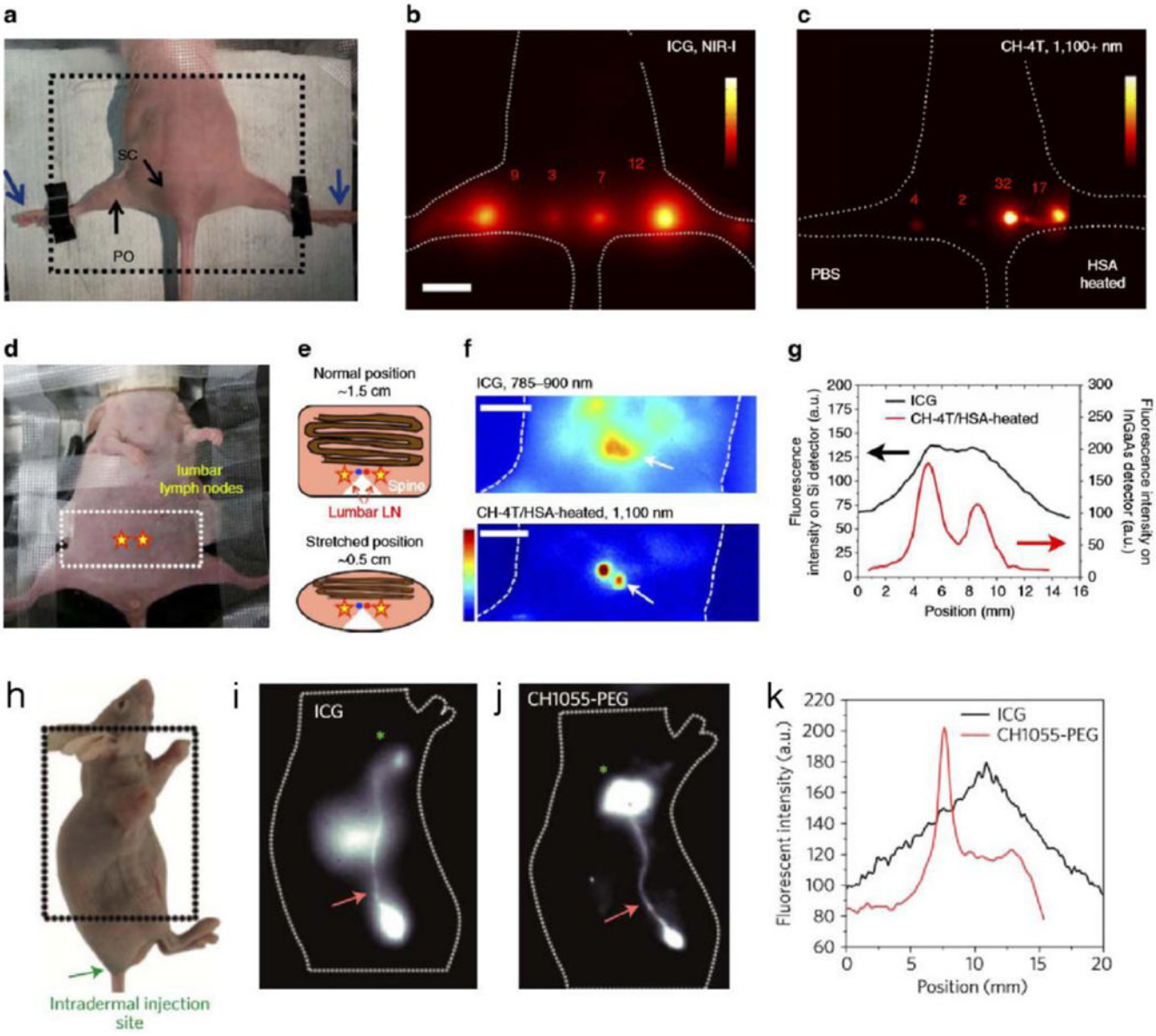

Figure 13. NIR-II lymph node imaging through NIR-II fluorophores.

a) Photograph of imaging position/field view of a nude mouse for popliteal and sacral lymph nodes imaging. b) NIR-I imaging with ICG showed much scattering of lymph nodes (imaging details: 16 $mWcm^{-2}$ 785-nm laser with 780 band-pass filter, silica camera, 50 ms). c) NIR-II imaging with either CH-4T/PBS (left foot) or CH-4T/HSA-HT (right foot) showed the sharp shape of the lymph nodes. Scale bar is 1 cm (imaging details: InGaAs camera, 1100 nm LP, 100 ms). d) Photograph of imaging position/angle for lumbar lymph nodes (yellow stars). e) Scheme of compressing mouse reduced the distance from 1.5 to 0.5 cm. f) NIR-I/II mapping of lumbar lymph nodes with the administration of ICG and CH-4T@HSA complex, respectively. Scale bar is 1 cm (imaging details: silica camera and 300 ms for ICG channel, InGaAs camera and 400 ms for CH-4T channel). g) Signal profiles of lumbar lymph nodes. Reprinted with permission from Ref. [72]. h) The photograph showed a

U87MG tumor-bearing nude mouse, with the intramuscular injection of ICG or CH1055-PEG. i–k) NIR-I/NIR-II imaging exhibited different imaging quality of inguinal lymph node and adjunctive lymphatic vasculature (imaging details: 850–900 nm and 100 ms for ICG, 1200 nm LP and 200–300 ms for CH1055-PEG). Reprinted with permission from Ref. [88].

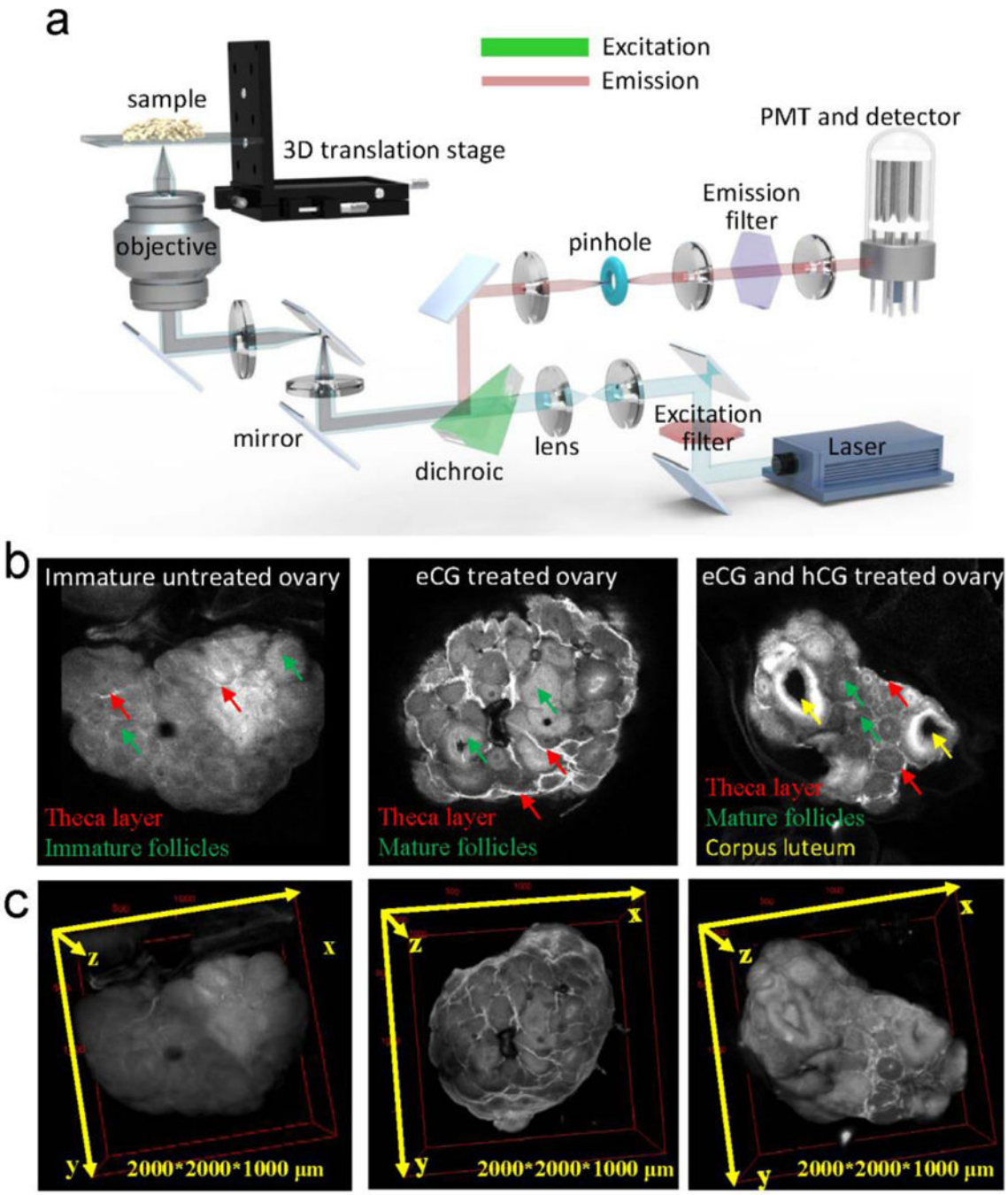

Figure 14. NIR-II confocal imaging.

a) Optical scheme of the first NIR-II confocal microscopy with the stage scanning approach. b-c) The NIR-II confocal microscopy enabled the 2D and 3D imaging of mouse ovary with improved penetration depth and contrast resolution. The 3D imaging can distinguish the stage development of ovary with recognizing the theca layer, mature granulosa cells, and corpora lutea cells (imaging details: 785 nm excitation, 1100 nm LP emission, laser power ~30 mW). Reprinted with permission from Ref. [18].

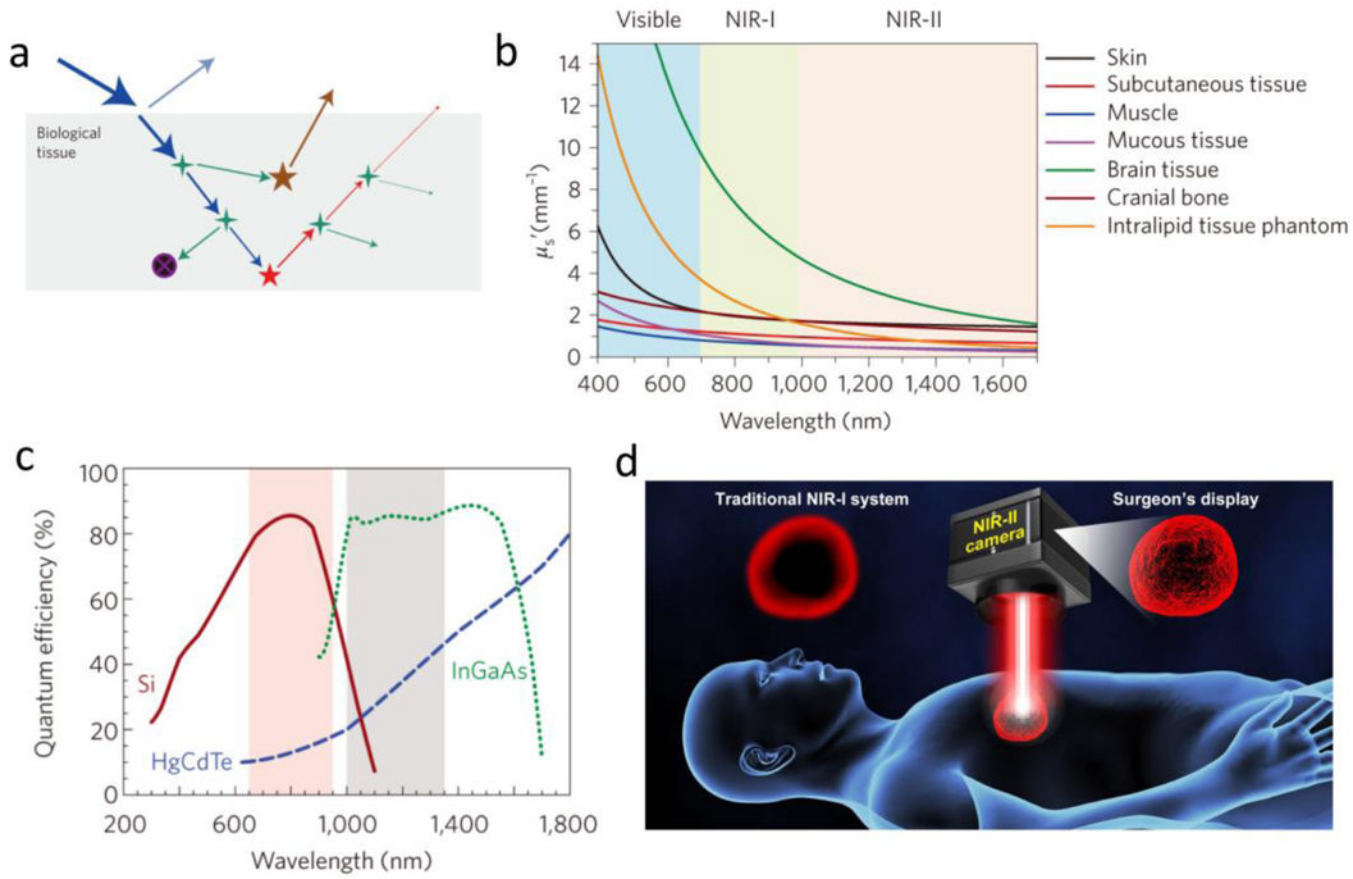

Figure 15. The reduced tissue autofluorescence and scattering are the motivation for developing NIR-II fluorescence-derived biomedical imaging.

a) Excitation laser-organ/tissue interactions include blue excitation light, cyan reflection, green scattering, black absorption, as well as brown autofluorescence. All of these parameters generate the loss of fluorescence and the gain of background signals (noise). b) Diminished scattering coefficients of different tissue phantoms as a function of wavelengths. c) Quantum efficiency curves for several cameras based on silicon, InGaAs or HgCdTe sensors. d) NIR-II guided imaging will improve the surgery accuracy with lower autofluorescence and scattering compared with NIR-I navigation system. Reproduced with permission from ref. [4] for a-b) and ref. [150] for c).

Table 1.

Typically reported peak and off-peak NIR-II fluorophores.

Fluorophore	Absorption/emission wavelength	Tissue targets	Properties	Applications	Refs
CH1055 and derivatives	750/1055 nm	Nonspecific; EGFR+	Water-soluble; QY=0.03% (NIR-II, IR26=0.05%)	Vessel imaging; lymph node imaging, tumor imaging	[88, 91, 92, 96, 97]
Fluorene-based D-A-D dyes (e.g. IR-E1)	830/1071 nm	Nonspecific; conjugatable with targeting ligands	Water-soluble; QY=0.07% (NIR-II, IR26=0.05%)	Brain vessel; TBI	[98]
IR-FGP	745/1050 nm	Anti-Neuron; $EGFR^+$	Water-soluble; QY=0.19% (NIR-II, IR26=0.05%)	Brain tissue Neuron imaging	[93]
IR-FEP	780/1047 nm	Nonspecific; conjugatable with targeting ligands	Water-soluble; QY=0.20% (NIR-II, IR26=0.05%)	Vessel and tumor imaging	[94]
IR-FEPC	782/1053 nm	Human Chorionic Gonadotropin (hCG) conjugate	Water-soluble; QY=0.26% (NIR-II, IR26=0.05%)	Ovary imaging	[18]
IR-FTAP	733/1048 nm	Nonspecific; conjugatable with targeting ligands	Water-soluble; QY=0.53% (NIR-II, IR26=0.05%)	Hindlimb vessel imaging	[95]
CH4T	738/1055 nm	Nonspecific	Water-soluble with FBS complex; QY=1.08% (NIR-II, IR26=0.05%)	Vessel imaging, lymph node imaging	[72]
IR-pFE	774/1010 nm	Nonspecific	Water-soluble; QY=1.65% (NIR-II, IR26=0.05%)	3D vessel imaging, tumor imaging	[99]
Flav 7	1026/1045 nm	Nonspecific	Water-soluble by micelles; QY=0.53% (NIR-II, IR26=0.05%)	Whole body imaging, vessel imaging	[63]
FD-1080	1064/1080 nm	Nonspecific	Water-soluble; QY=0.31%, 5.94% (complex) (NIR-II, IR26=0.05%)	Vessel imaging	[69]
IRT	742/1047 nm	Peptide conjugate for CD133	Water-soluble; QY=0.15% (NIR-II, IR26=0.05%,)	Tumor targeting imaging	[100]
IR-BGP6	736/1047 nm	Anti-PD-L1 conjugate	Water-soluble; QY=0.15% (NIR-II, IR26=0.05%,)	Tumor targeting imaging	[101]
IR-BEMC6P	725/1025 nm	RGD conjugate and octreotate conjugate	Water-soluble; QY=0.18% (NIR-II, IR26=0.05%,)	Tumor targeting imaging	[102]
IR-1048-MZ	980/1046 nm	Nonspecific	Binding with nitroreductase; QY=0.6% (NIR-II, IR26=0.05%,)	tumor hypoxia	[71]
Indocyanine green (ICG)	807/822 nm, tail emission to NIR-II region[72]	Plasma lipoprotein and atheromas; mostly non-specific	Negatively charged; lipophilic; QY=9.3% (NIR-I, serum)	Cardiovascular and lymphatic angiography; tumor imaging and IGS	[61]
IRDye800CW	774/789 nm, tail emission to NIR-II region[72]	Nonspecific; conjugatable with targeting ligands	Negatively charged; hydrophilic; QY=12% (NIR-I, serum)	Tumor imaging and IGS	[103, 104]
Zwitterionic cyanine dyes	772/788 nm (ZW800–1), tail emission to NIR-II region	$\alpha v\beta 3$ (with RGD)	Zwitterionic (neutral net charge); hydrophilic; QY=15.1% (NIR-I, serum)	Tumor imaging	[76]
NIR-AIE-dots	630/810 nm	Nonspecific	Water-soluble by encapsulation; 0.28% (NIR-II, IR26=0.05%)	3D vessel imaging, tumor imaging	[105]
IR-12N3 and other commercial cyanine dyes	766/788 nm, tail emission to NIR-II region	Nonspecific; EGFR+	Water-soluble	Vessel imaging, lymph node imaging, SCC tumor imaging	[73]
ZX-NIR	740/900 nm, tail emission to NIR-II region	Nonspecific	"turn-on" by H_2S	Colorectal cancer imaging	[106]

Fluorophore	Absorption/emission wavelength	Tissue targets	Properties	Applications	Refs
IR-775, IR-780, IR-783, IR-797, IR-806, IR-808	~770/~800 nm, second peak emission to NIR-Ib (900–1000 nm) region	Nonspecific	QY=0.5–0.65% (NIR-II, IR26=0.05%)	Vessel imaging, lymph node imaging, tumor imaging, Leaf vein imaging	[68]

Note: Quantum yields of all reported dyes in this review were recalculated based on IR26 = 0.05%.[20] The reported QYs was generally tested in aqueous solutions with the reference IR26 in 1,2-dichloroethane (DCE) or Hipco carbon nanotube in water. The commonly used QY value of IR26 is from 0.05 to 0.5% while the tested QY of Hipco carbon nanotube is from 0.04% to 0.4%.[18] As a result, it is important to recalculate the QY with the same conservative reference value.